SENSORS

A biomimetic elastomeric robot skin using electrical impedance and acoustic tomography for tactile sensing

K. Park[1], H. Yuk[2], M. Yang[1], J. Cho[1], H. Lee[3], J. Kim[1]*

Human skin perceives physical stimuli applied to the body and mitigates the risk of physical interaction through its soft and resilient mechanical properties. Social robots would benefit from whole-body robotic skin (or tactile sensors) resembling human skin in realizing a safe, intuitive, and contact-rich human-robot interaction. However, existing soft tactile sensors show several drawbacks (complex structure, poor scalability, and fragility), which limit their application in whole-body robotic skin. Here, we introduce biomimetic robotic skin based on hydrogel-elastomer hybrids and tomographic imaging. The developed skin consists of a tough hydrogel and a silicone elastomer forming a skin-inspired multilayer structure, achieving sufficient softness and resilience for protection. The sensor structure can also be easily repaired with adhesives even after severe damage (incision). For multimodal tactile sensation, electrodes and microphones are deployed in the sensor structure to measure local resistance changes and vibration due to touch. The ionic hydrogel layer is deformed owing to an external force, and the resulting local conductivity changes are measured via electrodes. The microphones also detect the vibration generated from touch to determine the location and type of dynamic tactile stimuli. The measurement data are then converted into multimodal tactile information through tomographic imaging and deep neural networks. We further implement a sensorized cosmetic prosthesis, demonstrating that our design could be used to implement deformable or complex-shaped robotic skin.

INTRODUCTION

Human skin has inspired the creation of robotic skin because it has various beneficial features for physical human-robot interaction (pHRI) environments. Human skin is the largest sensory organ, with an area of about 2 m^2, protecting our entire body from external influences (1). The skin has four types of mechanoreceptors to feel various tactile stimuli (2, 3). Also, human skin efficiently achieves large-area tactile sensing capability using cognitive processing and a few mechanoreceptors that have a large receptive field (4, 5). If there is a robotic skin replicating these unique features, it would allow the robot to interact with the environment like humans. Integrating these features in a single robotic skin system is challenging, but it will be substantially beneficial for future robotics in pHRI environments.

Many robotic skin systems have been introduced since tactile sensing has become an important issue for humanoids (6, 7), prostheses (8, 9), and social robots (10, 11). Most systems primarily focus on protection and large-area sensing functionalities. The most common approach has been the use of two perpendicular and stretchable electrode lines (row and column electrodes) to form an array of sensing elements where each intersection of row and column electrodes forms a single tactile sensor (12–14). This approach can achieve a large sensing area with a small number of electrodes, but practical limitations—such as fabrication complexity for a large and three-dimensional (3D) geometry, fragility, complex wiring, and repair difficulties—still need to be addressed. Another widely adopted approach has been the use of microcontrollers and digital communication to modularize the sensing elements (15, 16).

These module-based robotic skins can achieve high scalability and robustness by connecting each module via a serial bus and monitoring their functionality, but fragile wiring exposed to the outside and relatively large power consumption (about 30 mW/cm^2) are considered to be their major drawbacks (16).

Alternatively, Lee *et al.* reported a neuromimetic architecture that enables simultaneous transmission of thermotactile information through a single conductive material. This method also allows the robotic skin to achieve a scalable and damage-resilient structure (17). There are other approaches implementing large-area sensing functionality using stereo cameras (18) or accelerometers (19), but fulfilling these aforementioned features of human skin (protection, multimodal sensing, and scalability) has not been achieved, especially in terms of practical requirements such as durability, cost efficiency, and repairability.

Here, we report a biomimetic robotic skin based on hydrogel-elastomer hybrids and tomographic imaging (Movie 1). The goal of our work was to provide a robot with human skin–like features

| Biomimetic Robotic Skin | Deep pressure (EIT) | Dynamic Stimuli (PAT) |

Roller

Deformation

Trajectory

The developed robotic skin could sense deep pressure and dynamic stimuli in real-time, by using tomographic imaging methods.

Movie 1. Summary of study.

[1]Department of Mechanical Engineering, Korea Advanced Institute of Science and Technology, Daejeon, South Korea. [2]Department of Mechanical Engineering, Massachusetts Institute of Technology, Cambridge, MA, USA. [3]Institute of Smart Sensors, University of Stuttgart, Stuttgart, Germany.
*Corresponding author. Email: jungkim@kaist.ac.kr
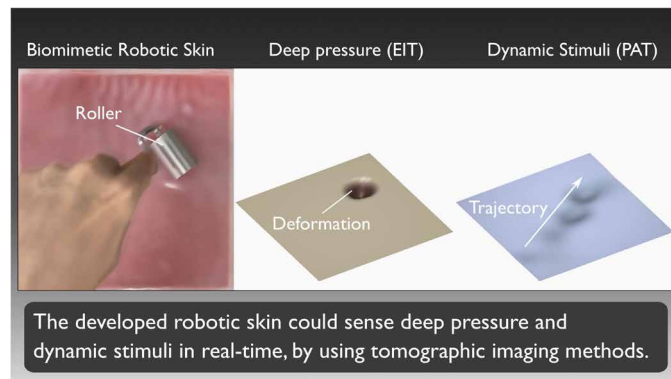
such as protection, multimodal tactile sensation, high scalability, and repairability. The developed robotic skin has a skin-inspired multilayer structure that consists of an ionic hydrogel and a silicone elastomer. The physical properties of the hydrogel are customizable and can be further improved through integration with silicone. The synergy between hydrogel and silicone allows the robotic skin to achieve not only skin-like softness but also high resilience for protection. The robotic skin can detect resistance changes and vibration using electrodes and microphones. These measurement data are subsequently used to reconstruct multimodal tactile sensation through tomographic imaging with the use of electrical impedance tomography (EIT) (20, 21) and passive acoustic tomography (PAT) (19, 22). Deep neural networks (DNNs) are also used to improve the reconstruction performance or to classify the touch modality based on vibration signals. The robotic skin is also robust to external impact because there is no wire inside the multilayer structure. Furthermore, we demonstrated that the tactile sensing capability can be easily restored even after incisional damage (23). By combining the multilayer structure and tomographic imaging, we developed a robotic skin that resembles human skin in structure, function, and working principle. We further implemented a sensorized cosmetic prosthesis to demonstrate the potential of the proposed robotic skin.

RESULTS

Biomimetic multilayer structure with distributed sensing elements

Human skin is composed of three primary layers (epidermis, dermis, and hypodermis), which have different characteristics and functions. The epidermis is the outermost layer of the skin that forms a waterproof barrier to prevent dehydration. The epidermis layer has a Young's modulus of about 2 MPa, which is considerably high (24). The dermis is an elastic layer that lies beneath the epidermis. This layer consists of elastic tissue and fibers, giving skin resilience and toughness. The reticular dermis can be stretched up to 25% owing to the collagen fibers that ensure full recovery of tissue shape and structure after deformation (25). The dermis is physically interlocked with the epidermis, so they are not sliding over each other even under the shear force. It also creates a spatial filtering effect that spreads forces and pressure across a large area (26, 27). Last, the hypodermis (also called subcutaneous layer) is a thick and highly deformable layer found between the dermis and fascia. The hypodermis mainly consists of soft loose connective tissues (areolar tissue and adipose tissue), and their mechanical properties allow the skin to efficiently absorb and attenuate external pressure. Although it is not a part of skin, its structure and function are closely related to those of the dermis. Four primary tactile mechanoreceptors are also located in different layers in human skin. Merkel's disks and Meissner's corpuscles are located toward the surface of the skin. Ruffini endings and Pacinian corpuscles are located deeper inside the skin (28); they are often found in deep fascia, which is located beneath the hypodermis (29, 30).

Inspired by the structure of human skin, we create a biomimetic robotic skin consisting of four parts: elastomeric skin, a hydrogel layer, a base layer, and distributed sensing elements (Fig. 1A). The outermost layer of the sensor is elastomeric skin, which is made of stretchable and tough silicone rubber. The hydrogel layer is a compliant layer located underneath the elastomeric skin. The base layer

is a flexible plate coated with silicone rubber, and it is placed below the other layers to support them. These three layers are strongly cross-linked to each other so that those layers are not delaminated during physical interaction (31). For multimodal tactile sensing, the electrodes and microphones are placed between the base layer and the hydrogel layer. We use this configuration to replicate some beneficial features of human mechanoreceptors.

The proposed structure offers several advantages for robotic skin. First, the robotic skin would have a protective function for safe human-robot collaboration, owing to the mechanical properties of the hydrogel-elastomer hybrids (Fig. 1B). The multilayer structure has a spatial filtering effect that offers a cushioning function of the skin. The compliance of the hydrogel provides a dampening effect from external force, whereas the elastomeric skin withstands the force and spreads it to a larger area (fig. S1). In addition, we can customize the geometries and/or mechanical properties of the multilayer structure to achieve an appropriate elastic modulus and thickness of the robotic skin; it would enable the robotic skin to fulfill safety criteria for various injuries, such as contusion (energy density, <2.52 J/cm^2) and laceration (tensile stress, <1 MPa) (32). If the sensor is made only with the hydrogel, then deformation occurs locally in a small area so the sensor would not offer a sufficient protection. Because this protective function is realized by the mechanical properties of the multilayer structure, it is not impaired by the sensing characteristics (sensitivity and bandwidth). In addition, the elastomeric skin prevents direct contact between the hydrogel and air, offering an antidehydration effect. Specifically, the elastomeric skin effectively mitigated moisture loss of the hydrogel (fig. S2) over 60 days without noticeable changes in sensing performance or the need of retraining in machine learning algorithm. The long-term stability of the system can potentially be improved by the use of elastomers with much lower water permeability, such as butyl rubber (33) and/or nonvolatile ionic hydrogels (34).

The hydrogel layer can also be used as a medium for tactile sensing (Fig. 1C). Hydrogels contain a large amount of water and have electrical conductivity because of the presence of electrolytes (fig. S3) (35). We also demonstrated that hydrogels transmit the vibration generated by touching the surface to the entire multilayer structure. These properties allow us to deploy electrodes and microphones on the base layer and use them to measure the force and vibration applied to the sensor's surface. The developed robotic skin is able to detect not only weak vibrations but also forces up to 20 N (figs. S4 and S15), which is sufficient to sense typical human touch interaction such as a stroke or push (36).

The distributed sensing elements allow the robotic skin to achieve high scalability (Fig. 1D). Each sensing element has a large receptive field so that the robotic skin can achieve a large sensing area with a small number of sensing elements. In addition, the sensing elements can be freely arranged within a large, curved, and even deformable surface. Because there is no direct connection between the sensing elements, we can incorporate an additional sensing element without concern about the existing sensing elements. This feature allows us to easily adjust the size of the robotic skin.

In addition, the robotic skin has the ability to repair after damage without loss of its functionality (Fig. 1E). If excessive force is applied to the robotic skin, the multilayer structure may become locally lacerated or crushed, causing the robot skin to lose its sense of touch. The proposed design does not expose any wires, whereas other approaches expose wires or circuits externally. We have
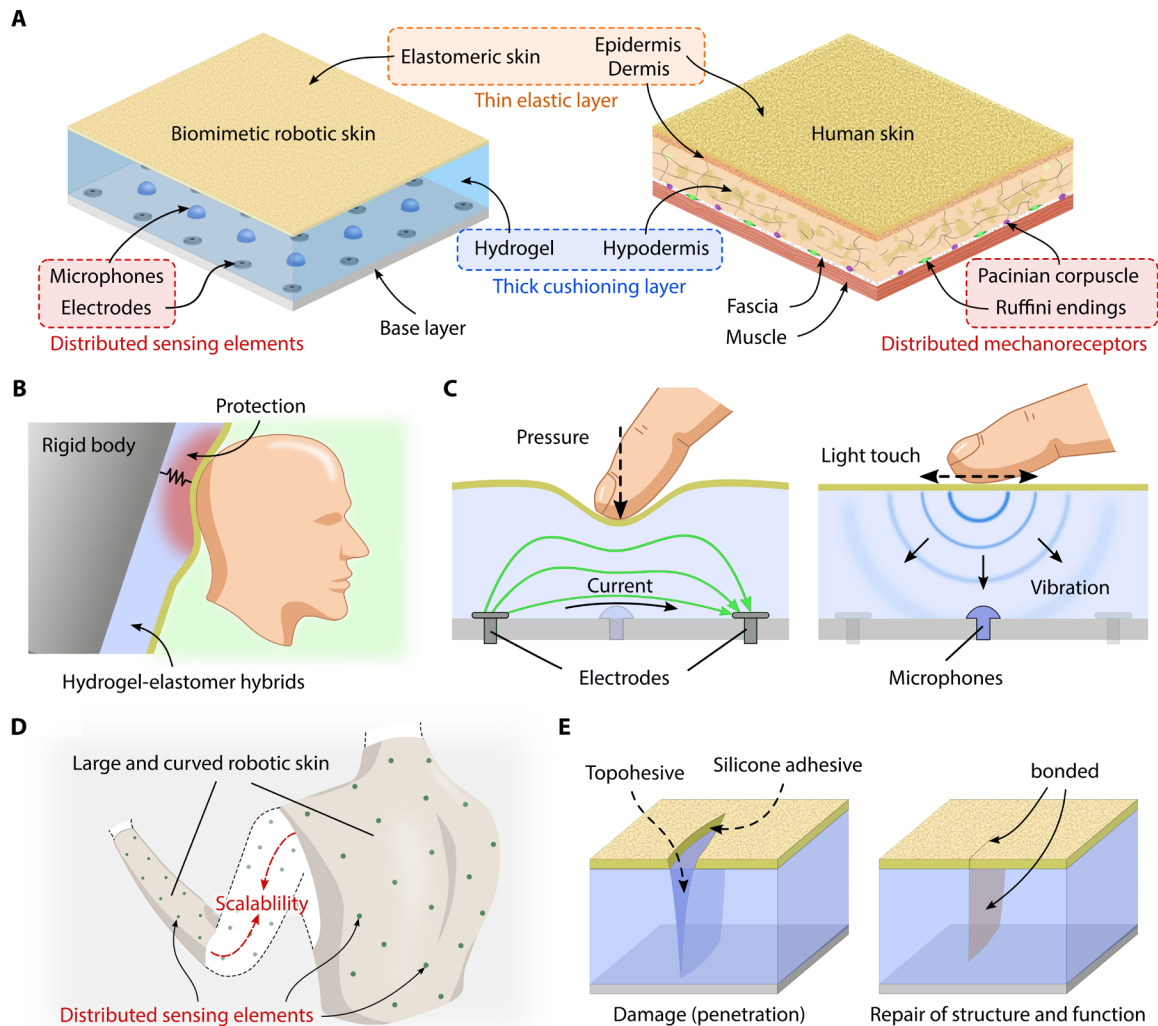
Fig. 1. Concept of biomimetic multilayer structure for robotic skin. (**A**) Comparison between the biomimetic multilayer structure based on hydrogel-elastomer hybrids and human skin. Both structures consist of an elastic and tough outermost layer (elastomeric skin and dermal layer) and a thick and compliant cushioning layer (hydrogel and hypodermis). Sensing elements were also evenly distributed deep in the multilayer structure. (**B**) The multilayer structure allows the robotic skin to achieve an appropriate material property and dimensions for the protection function. (**C**) Because the hydrogel layer is compliant and electrically conductive, it can be used as a pressure-sensitive material. In addition, dynamic tactile stimuli (light touch) can be measured by detecting vibrations generated on the surface and transmitted through the multilayer structure. (**D**) Scalable design based on distributed sensing elements with a large and overlapping receptive field. (**E**) The biomimetic robotic skin can be repaired with an adhesive after damage to restore its structure and function.

demonstrated that the robotic skin is repairable by restoring the electrical and mechanical properties of the multilayer structure using an adhesive for hydrogel or silicone rubber (*37*, *38*).

Deep pressure sensing based on EIT

To sense deep pressure, we used the hydrogel as a pressure-sensitive material. The hydrogel is electrically conductive, and it is deformed when a force is applied. The impedance between electrodes was altered depending on the cross-sectional area for current to flow, which was reduced due to indentation. The results showed that the electrical impedance increased proportionally to the indentation depth (fig. S4). There was no dead zone, and the limit of detection was about 0.7 N. Hydrogels also exhibit low piezoresistive hysteresis (less than 3%) because the piezoresistive mechanism is based on

changes in geometry (cross-sectional area for current flow) rather than changes in the percolation network (*39*).

Because the pressure was locally applied to the robotic skin, the conductivity distribution of the hydrogel was found to be locally altered accordingly. The location and intensity of the deformation can be observed using EIT, a nondestructive imaging technique that has been widely used for medical imaging (*40*, *41*), geophysical exploration (*42*), and human-machine interfaces (*43*, *44*). Figure 2 demonstrates how the proposed robotic skin senses deep pressure using EIT. The metal electrodes were evenly placed between the hydrogel and the base layer, so the local deformation of the thick hydrogel layer can be indirectly measured using the electrodes (Fig. 2A). An alternating current of 40 kHz was injected through a pair of electrodes, and the resulting voltage was measured across
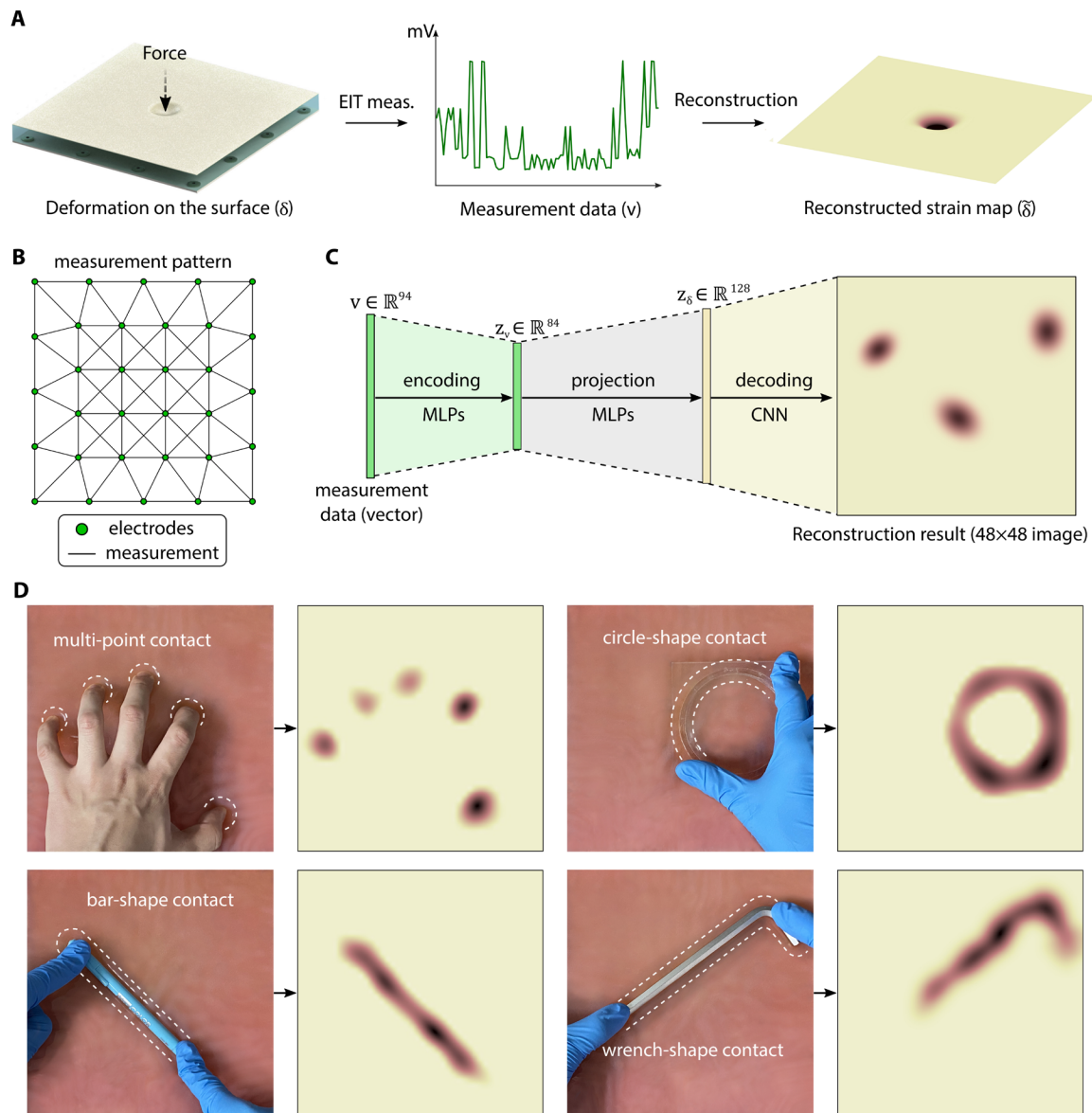
Fig. 2. Deep pressure sensing using EIT. (**A**) Sensing procedure for deep pressure using EIT. The measurements were conducted across the electrodes, and these data were used to reconstruct the deformation map due to deep pressure. (**B**) Optimal measurement pattern for the developed robotic skin. The green circles and black lines indicate the electrodes and measurement pair, respectively. The electrode arrangement was heuristically determined so that 32 electrodes were spaced as evenly as possible in a square area. (**C**) Deformation map was reconstructed from measurement data through DNN-based EIT algorithm. (**D**) Image reconstruction results for various shapes of deep pressure (multipoint contact, circle-shaped contact, bar-shaped contact, and wrench-shaped contact).

that pair. We used an alternating current to minimize the double-layer capacitance at the interface between the electrodes and electrolyte (*45*). The measurements were then repeated on other pairs of electrodes along the predefined measurement pattern (Fig. 2B). Last, the measurement data were converted into a deformation map using an EIT reconstruction algorithm.

There are various inverse solving algorithms for implementing EIT (*46*, *47*), but most of them have a trade-off between accuracy and speed (text S1). Thus, we used an EIT reconstruction algorithm based on a DNN, which has shown promising results in terms of accuracy, noise robustness, and reconstruction speed (Fig. 2C and fig. S6) (*48*, *49*). In this method, a measurement vector was mapped

into the latent variable through multilayer perceptron (MLP), and a deformation map was generated from the latent variable through a convolutional neural network (CNN). The network was trained using simulation data because it is impractical to obtain measurement data by experiments.

To demonstrate the EIT reconstruction performance, we pressed the biomimetic robotic skin with a hand or objects of various shapes and obtained the reconstruction results through the DNN-based EIT algorithm (Fig. 2D and movie S1). The result shows that the trained network can reconstruct deformation maps of various shapes. This result is notable considering that the spacing of the electrodes is about 40 mm (0.08 U/cm^2). This design could be implemented

because of the large and overlapping receptive fields of the EIT measurement pattern. A single-point indentation experiment was also conducted to evaluate the contact localization accuracy, and the single-point contacts could be localized with a root mean square (RMS) error of 4.2 mm (figs. S8 and S9). This demonstrates that the EIT allows the robotic skin to achieve tactile superresolution through the interpolation between overlapping receptive fields.

Dynamic tactile sensing method based on PAT

Human skin also perceives dynamic tactile stimuli through vibration-sensitive mechanoreceptors (Pacinian corpuscles). The vibrations are usually generated on skin surfaces by dynamic tactile stimuli, and they are transmitted and recognized by the Pacinian corpuscles. Our biomimetic robotic skin senses the dynamic stimuli in a similar way. If dynamic stimuli are applied to the elastomeric skin,

microvibrations are generated and transmitted deep into the sensor through the multilayer structure. The vibrations can be detected by the microphones that are evenly distributed over the base layer (Fig. 3A). Each microphone was also encased in a silicone capsule so that it could sense vibrations generated from a distance of about 5.5 cm (fig. S15). Owing to the large receptive field, the robotic skin could detect stimuli over a large area with a low receptor density (0.0625 U/cm^2).

Because the energy of vibrations is gradually attenuated as they are propagated, the vibration intensity of each microphone is determined by its distance from the vibration source. Thus, we calculated the position of the dynamic stimulus by applying PAT to the difference in signal strength obtained from each microphone (Fig. 3B and text S2). Each microphone continuously measures the vibration due to touch, and the signal intensity is defined as the power of the
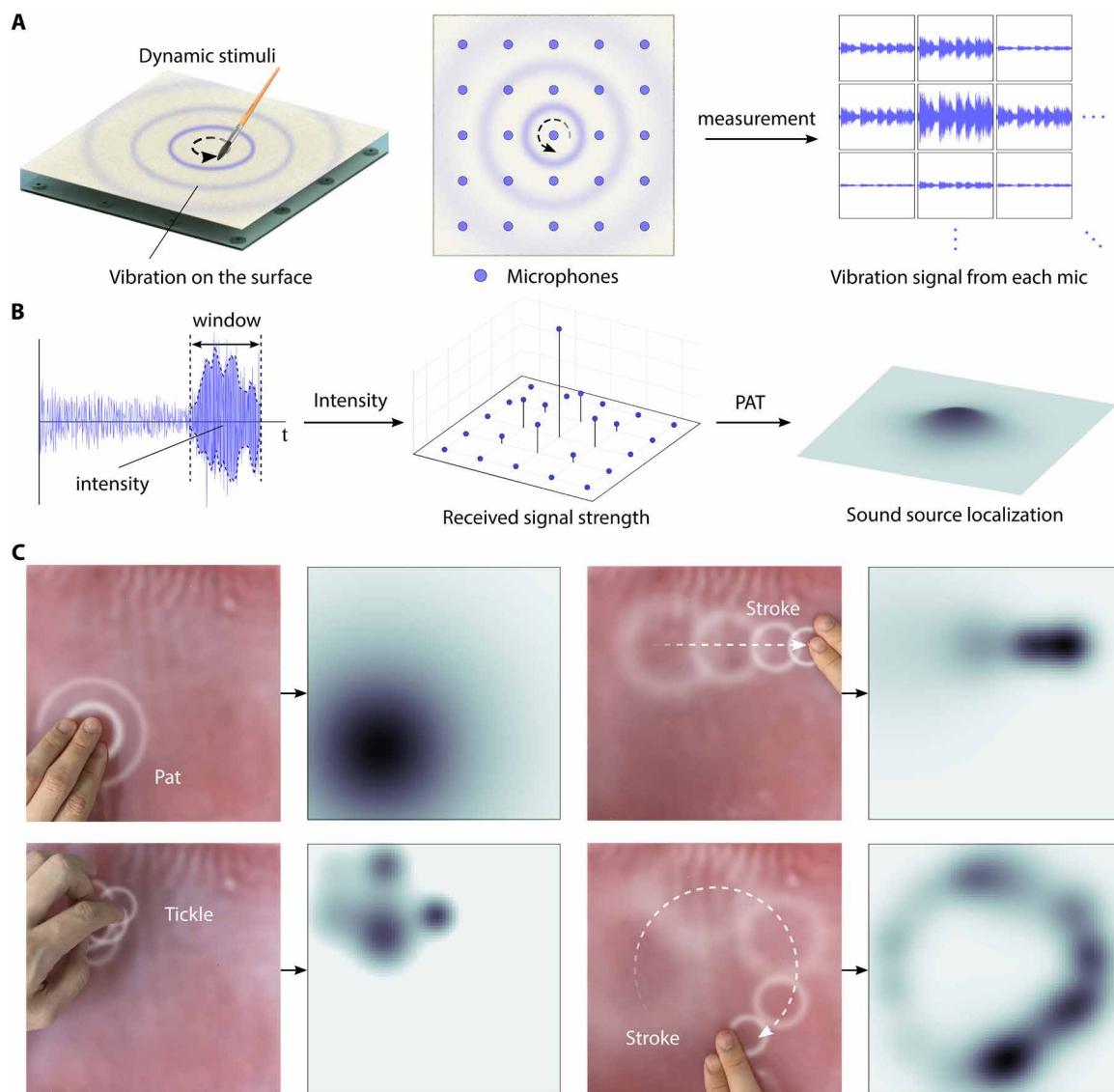
Fig. 3. Dynamic tactile sensing using PAT. (**A**) Measurement of dynamic tactile stimuli using an array of microphones. The microphones were placed as evenly as possible in the remaining space where the electrodes were placed. (**B**) Localization of dynamic tactile stimuli using PAT and differences in received signal strength. (**C**) Localization of dynamic stimuli (pat, tickle, and strokes) and their trajectories.

signal within a specific time window. Then, the location of the contact (vibration source) is estimated by minimizing the cost function derived from the decaying model of the vibration.

To demonstrate the localization algorithm, we applied various dynamic tactile stimuli (pat, tickle, and stroke) to the robotic skin, and the PAT algorithm was used to localize the stimuli (Fig. 3C and movie S1). Each image frame was filtered using a weight decaying over time to visualize the trajectory of the stimuli. The results showed that the robotic skin could successfully sense and localize dynamic tactile stimuli using microphones and PAT. To evaluate the localization accuracy, we carried out another experiment whereby we applied a light touch repeatedly to a single point and localized its position using the PAT algorithm. The results showed that the stimulus could be localized with an RMS error of 6.6 mm (fig. S8).

Touch modality classification using CNN

Humans perceive tactile stimuli through the skin and often interpreted these stimuli as social cues or haptic signals with intent. Such a touch modality can be determined according to the intensity, location, and pattern of stimulus. For instance, a tickle consists of repeated light touches, and a stroke produces a continuous and moving vibration pattern. Each stimulus also has its own unique tone. These touch modalities provide additional meaning to simple tactile data such as force or vibration, facilitating tactile communication.

The robotic skin is also able to classify dynamic tactile stimuli (tap and tickle) based on the features of vibration signals because the type of touch determines the spatiotemporal pattern of the vibrations (Fig. 4). First, a history of the vibration intensity from each microphone was obtained. Second, a spectrogram was obtained from the most notable channel to observe the frequency spectrum over time. These 2D arrays were combined to form a feature image that represents the spatiotemporal pattern of the vibrations. Then, the dynamic tactile stimuli could be classified by applying a CNN to the feature image (fig. S7).

To evaluate the classification accuracy, we conducted an experiment to classify touch modality using real measurement data. A dataset from 10 individuals was collected, where each person was asked to continuously apply four dynamic tactile stimuli (pat, tickle, stroke, and wind blow using an air brush). Five hundred feature images for each stimulus were collected from each participant, resulting in 5000 feature images for each stimulus. An equal number of feature images of baseline noise, where no contact is made on the skin, were added to the dataset. The collected dataset was also augmented by a factor of 5 by adding Gaussian noise. Last, the collected dataset was randomly divided into training, validation, and test sets at a ratio of 8:1:1 to avoid overfitting. The trained network classified the test set with an accuracy of 98.7%.

For demonstration, the trained neural network was used to classify the touch modality in real time (movie S2). Dynamic stimuli
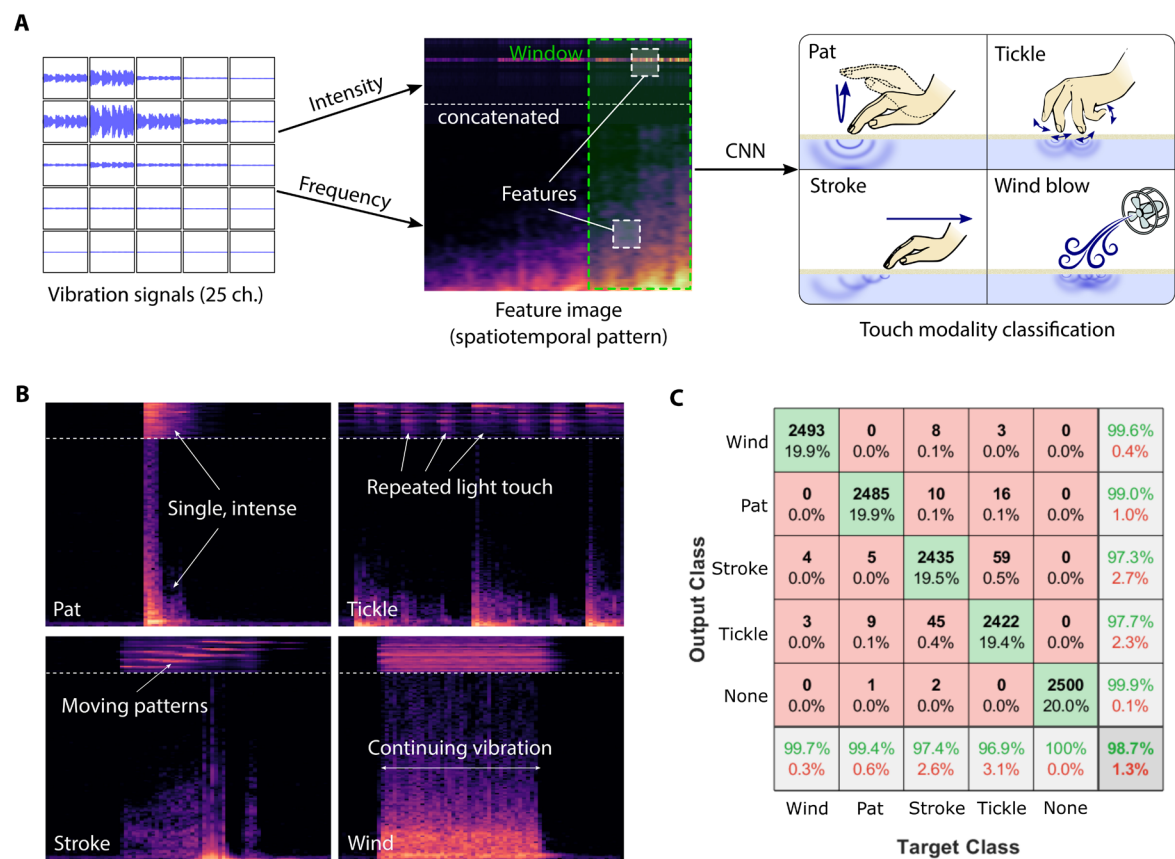
Fig. 4. Classification of dynamic tactile stimuli based on spatiotemporal features of vibration. (**A**) A feature image was defined by concatenating the intensity history and spectrogram, which were obtained from the microphones. Subsequently, the spatiotemporal pattern of vibrations was extracted from the feature map using a CNN to classify the stimuli. (**B**) Examples of the feature images (pat, tickle, stroke, and wind blow). (**C**) Confusion matrix of the classification results.

were applied to the developed robotic skin to obtain a feature image. Then, the pretrained neural network classified the touch modality based on the feature image in real time. The length of the time window was 0.5 s, and classification was performed every 0.1 s. The result shows that the trained network successfully classified the touch modality; thus, the developed robotic skin is capable of haptic communication with humans by understanding the intention of the touch.

Repair and restoration of the robotic skin

The developed robotic skin is robust to local damage and repairable. The electrodes and microphones are not directly exposed to external force, so the robotic skin is not totally disabled although the elastomeric skin or hydrogel is damaged (Fig. 5B). The sensor structure can also be easily repaired using adhesives for hydrogels and elastomers. We have demonstrated this repairability. The developed robotic skin was cut with a scalpel, resulting in a loss of electrical connectivity and the inability to detect signals on the skin surface (Fig. 5A). Although the robotic skin was locally disabled due to damage, the tactile sensing capability did not deteriorate at the periphery of the site of damage (Fig. 5B). This result shows that the proposed design is robust to local damage. To repair the robotic skin, we bonded the hydrogel layer using a chitosan topohesive (37, 50). An aqueous solution of chitosan was used to bond hydrogel, and it was placed within the defect for a duration of 30 min (Fig. 5C). The chitosan chains cross-link into a polymer network in topological entanglement with the networks of the cut surfaces. When the cut surfaces adhere sufficiently, the silicone skin is fixed using commercial sealant (Fig. 5D). After repair, the joined part showed a stable

electrical connection again even under deep pressures (Fig. 5E). The repaired robotic skin could localize the force applied to the repaired area, and no artifacts were observed in the reconstructed images (movie S3). Furthermore, the electrical and mechanical connection of the repaired region was stable even under the external force of 20 N (fig. S13). This demonstrates that the structure and function of biomimetic robotic skin can be recovered in an easy and simple procedure.

Application on a sensorized prosthesis

Because we can freely customize the shape of the hydrogel-elastomer hybrid and the arrangement of the sensing elements, the developed biomimetic robotic skin can be easily realized on a large and curved surface. To demonstrate this advantage, we made biomimetic robotic skin for a prosthesis as a proof of concept. The prosthesis was capable of sensing deep pressure through EIT (movie S4). The sensorized prosthesis (cosmetic prosthesis) consisted of an elastomeric skin, ionic hydrogel, and a rigid core with metal electrodes (Fig. 6). Because there is some space inside the rigid core, we expect that the proposed design can be easily integrated into the motorized system. There are currently several challenges in restoring sensory feedback to individuals with impaired sensation due to disease, trauma, or amputation. The proposed robotic skin offers a platform that could be integrated with devices such as prostheses to provide a means for end users to physically interact with their surroundings.

DISCUSSION

We introduce a biomimetic robotic skin emulating the characteristics of human skin. The design of the multilayered structure with
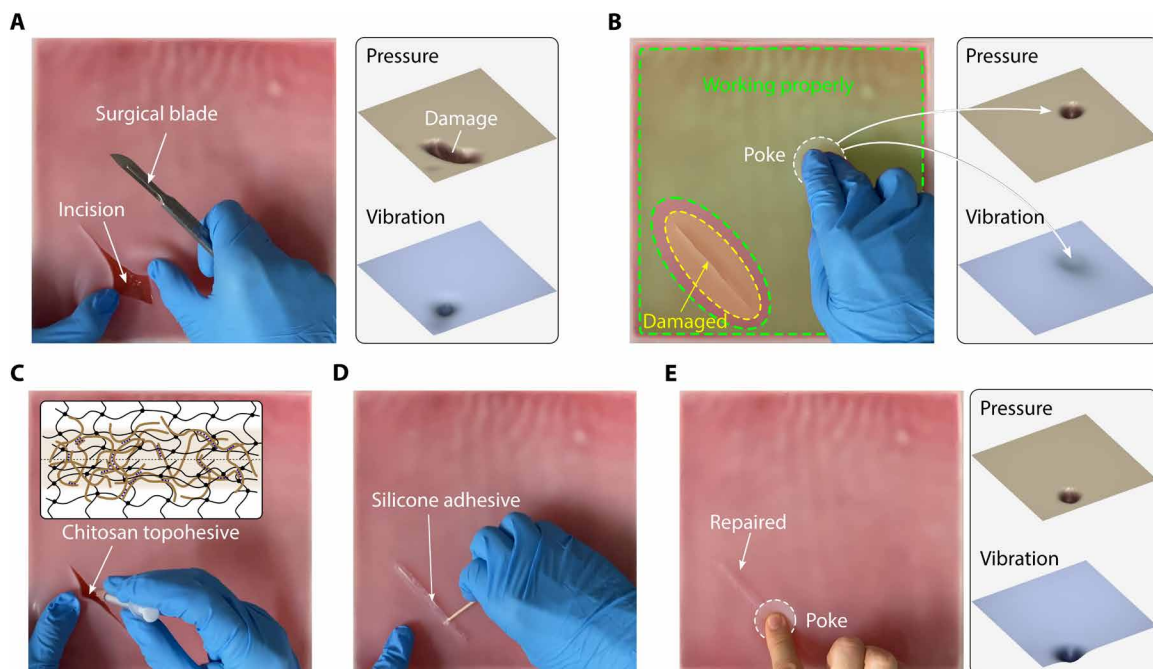
Fig. 5. Repairability of the robotic skin. (**A**) The robotic skin was cut with a surgical scalpel. The incision resulted in a local loss of electrical connection, which can be observed through the EIT. (**B**) The robotic skin was locally disabled from tactile sensing due to the damage, but the peripheral regions surrounding the defect remained functional. (**C**) Chitosan topohesive was applied to the damaged region to bond the hydrogel. Cross-linking of the polymer network was achieved in a pH-responsive technique, thereby bonding the cut surfaces. (**D**) Elastomeric skin was fixed with a silicone adhesive (room temperature–vulcanizing rubber). (**E**) The structure and tactile sensing functionality of the robotic skin were restored, including the region with the defect after repair.
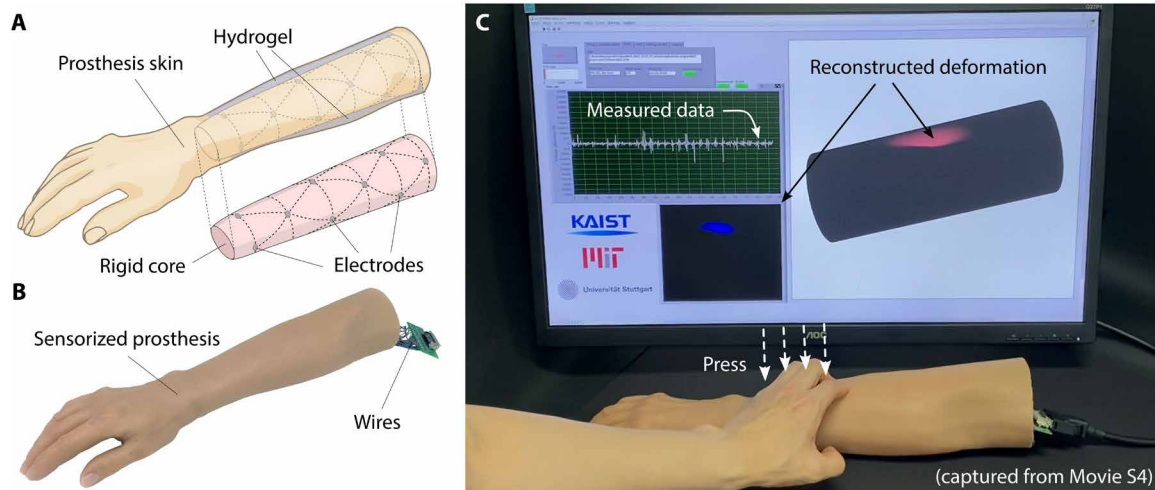
Fig. 6. Application of the biomimetic robotic skin to a cosmetic prosthesis. (**A**) Structure of the sensorized prosthesis. The rigid core includes metal electrodes to perform EIT-based tactile sensing. A hydrogel layer was formed between the rigid core and prosthesis skin, and it was used as a pressure-sensing material. (**B**) An image of the prosthesis incorporating the robotic skin. (**C**) Demonstration of EIT-based tactile sensing on the prosthetic arm.

distributed sensing elements enables large-area tactile sensing over continuous and curved surfaces, as shown in Fig. 6. Although other methods can achieve this level of tactile sensing performance, the tomographic imaging approach successfully achieves complex curved robotic skin with a relatively simple and practical manufacturing process.

The hydrogel-elastomer hybrid is able to prevent soft tissue injuries from occurring to humans owing to its mechanical properties (*32*). This robotic skin would provide robots with a tactile sensation, allowing the robot to move to ensure safety. Although the resultant multilayered structure might be relatively heavier than other materials such as foams, the robotic skin can offer close replication of the feeling of human skin (*51*). This feature is expected to be critical for building empathy and attachment in social robots.

The proposed robotic skin could sense deep pressure and dynamic tactile stimuli through EIT and PAT. These tomographic imaging methods are simultaneously implemented in a biomimetic multilayer structure and complement each other synergistically. This approach also allows the robotic skin to be realized with a low receptor density. The sensing performance shown in Figs. 2 and 3 demonstrates that the developed robotic skin can detect moderate levels of multipoint contacts from light vibratory touch to strong deep pressure. However, the current system cannot distinguish various deformations such as normal indentation and stretch because these deformations had not been considered during the training of the DNN. Nonetheless, such additional deformation regimes can be included by introducing a material with anisotropic resistivity (*52*) or augmenting the training dataset with simulation results regarding various deformations. It would also be possible to augment the sensing modality by adding artificial intelligence–based sensing methods with different transducing principles such as optical (*53*) and magnetic (*54*).

The touch modality could also be classified with an accuracy of 98.7% as shown in Fig. 4, which shows the potential of the developed robotic skin in haptic communication between humans and robots. We also envisage that the number of classifiable modalities can increase if we improve the feature images to include EIT data.

We also demonstrated that the biomimetic robotic skin can be restored after severe damage. This repairability is a practical and necessary feature of robotic skin for pHRI; however, the repair process still has to be conducted manually. In the future, the use of self-healing materials could be explored to more closely mimic human skin (*55*, *56*).

In summary, we have developed a robotic skin by taking inspiration from the native human skin in terms of its architecture and functionality. The proposed design approach can also be further developed by integrating with other transducing methods such as capacitive, magnetic, or optical methods. This study presents an alternative yet practical approach for creating large-area robotic skin, and we envisage that our study would help robots to interact with their environment.

MATERIALS AND METHODS
Fabrication of the biomimetic robotic skin
The sensing domain of the robot skin measures 20 cm by 20 cm. The base layer was prepared by cutting an acrylic plate using a laser cutter (Speedy 300, Trotec), and its surface was coated with a silicone elastomer (Dragon Skin 20, Smooth-On). The electrodes were low-head stainless bolts (CBSTSR4-8, Misumi), which were used for EIT. The surface of the electrodes was functionalized using 3-(trimethoxysilyl) propyl methacrylate to form a stable connection between the hydrogels (*57*). The condenser microphones (CMEJ-4622-25-L082, CUI Inc.) were used to capture the vibration. Thirty-two electrodes and 25 microphones were evenly distributed on the base. The electrodes were firmly fixed on the base layer. The microphones were encapsulated with a silicone elastomer (Dragon Skin 20, Smooth-On) and bonded to the silicone surface of the base layer. The silicone surface and the elastomeric capsules were treated with a 10 weight % (wt %) benzophenone (BP)–ethanol solution, so they could be strongly bonded to the hydrogels through an ultraviolet (UV)–initiated polymerization process.

The biomimetic multilayer structure was made of a silicone elastomer and tough hydrogel (fig. S5). The thicknesses of the elastomeric

skin and the hydrogel were 500 μm and 1 cm, respectively. The elastomeric skin was a large film made with a silicone elastomer (Dragon Skin 20, Smooth-On), and it was treated with a BP-ethanol solution. Other silicone-based parts were also treated with BP solution for the same reason. The hydrogel layer was prepared by mixing a degassed aqueous precursor solution of a polyacrylamide-alginate (PAAm-Alg) tough hydrogel [13.2 wt % acrylamide, 0.8 wt % sodium alginate, 0.02 wt % MBAA (N',N'-methylenebisacrylamide), and 0.2 wt % Irgacure 2959] and calcium sulfate slurry (0.1328 times the weight of sodium alginate). The mixture was mixed quickly and poured onto a BP-treated sensor base. Then, the mixture was covered with BP-treated elastomeric skin to prevent contact with oxygen. We waited 1 hour for the alginate to cure primarily, and then cured the polyacrylamide in the UV cross-linker (CL-3000L, Analytik Jena) for 1 hour. Because all the elements of the robotic skin were chemically treated for bonding with the hydrogel, the developed sensor did not fail or delaminate under external forces.

The sensorized prosthesis is composed of an elastomeric skin (cosmetic prosthesis, Regal) and a rigid core, and the gap between the two parts is filled with tough hydrogel. The inner side of elastomeric skin was treated with a BP-ethanol solution and coated with a PAAm hydrogel (58). The tough hydrogel was prepared by mixing a precursor solution of PAAm-Alg hydrogel [13.2 wt % acrylamide, 0.8 wt % sodium alginate, 0.008 wt % MBAA, 0.0465 wt % APS (ammonium persulfate), and 0.033 wt % TEMED (tetramethylethylenediamine)] and a calcium sulfate slurry (0.1328 times the weight of sodium alginate). The mixture was mixed with a frother and injected using a syringe into the gap between the elastomeric skin and the rigid core. The cosmetic prosthesis was then placed in a water tank to prevent contact with oxygen through the gas-permeable skin. We waited 1 hour for the precursor solution to cure. The hydrogel precursors infiltrated into the hydrogel-coated surface, forming an interpenetrating polymer network during the polymerization process (fig. S14). The materials used were as follows: alginate (Sigma-Aldrich, W201502), acrylamide (Bio-Rad, 1610140), MBAA (Sigma-Aldrich, M7279), TEMED (Sigma-Aldrich, T7024), calcium sulfate (Sigma-Aldrich, C3771), ammonium persulfate (Sigma-Aldrich, A3678), and 2-hydroxy-4′-(2-hydroxyethoxy)-2-methylpropiophenone (Irgacure 2959; Sigma-Aldrich, 410896).

Preparation of chitosan topohesive
The chitosan topohesive was prepared as described in the paper of Yang et al. (50). An acidic buffer solution was prepared by dissolving 0.976 g of 4-morpholineethanesulfonic acid powder (MES hydrate; Sigma-Aldrich, M8250) into 50 ml of deionized water. Sodium hydroxide (Sigma-Aldrich, S5881) was also added to the buffer solution until its pH reached 4.5. Then, chitosan powder (Sigma-Aldrich, 448877) was added to the solution and thoroughly mixed until the chitosan powder was completely dissolved.

Setup and procedure of indentation experiment
To evaluate the localization performance of the developed robotic skin, we conducted experiments in which tactile stimuli such as pressure or vibration were applied to the sensor surface. The experimental setup is presented in the Supplementary Materials (fig. S9). The plane-shaped robotic skin was placed on a three-axis motorized linear stage (EzRobo-5GX, Iwashita Engineering), and tactile stimuli were applied with an indenter or a vibrator unit depending on the experiment. The first experiment was to apply force to the robotic

skin with an indenter to evaluate the EIT-based contact localization performance. The indenter unit consists of a load cell (651AL, KTOYO) and a hemispherical tip with a diameter of 15 mm. The robotic skin was indented at each node of a 15 × 15 square grid, and the indentation depth was about 7.5 mm (75% of the thickness). During the experiment, the force value, the sensor output, the position of the indenter, and the indentation depth were all recorded. Then, deformation maps were reconstructed from the experimental data, and the localization performance was evaluated by comparing the peak positions with the actually indented positions (fig. S8). The second experiment was to apply vibration to the robotic skin with a vibrator to evaluate the PAT-based vibration localization performance. The vibrator consists of a voice coil motor (LVCM-032-076-02, Moticont), a cross roller guide (VR3-100X14Z, THK), a spring, and a rubber tip. The vibration was applied to a 13 × 13 square grid on the sensor surface, and the frequency of the vibration was 10 Hz. The dynamic tactile stimuli were localized by applying the PAT algorithm to the intensities of the recorded vibration signals, and the results were compared with the actual contact location (fig. S8).

Setup and procedure for cyclic loading
We conducted a cyclic loading test to investigate the mechanical and piezoresistive properties of the hydrogel-elastomer hybrids. A simple specimen representing the transducing mechanism of the multilayer structure was repeatedly indented using a hemispherical tip with a diameter of 15 mm (fig. S4A). The specimen was prepared with the following dimensions: 40 mm in width, 55 mm in length, and 10 mm in thickness. The electrodes had a radius of 3 mm and were spaced 43 mm from each other. Specimens were compressed up to 8 mm (80% of thickness), and the loading frequency ranged from 0.001 to 4 Hz. During the experiment, the indentation depth, resistance, and force values were continuously recorded, and the signals are processed with a first-order IIR LPF with a 3-kHz cutoff frequency. The result shows that the impedance between two electrodes increases in proportion to the applied force (fig. S4B). The hysteresis of the specimen was quantified by analyzing the loading/unloading curves, and the result shows that the hydrogel-elastomer hybrids exhibit low hysteresis (fig. S4, E and F). The limit of detection was also defined as the force value that changed the sensor output by three times the SD of the measurement noise, and the value was found to be about 0.7 N.

In addition, the cyclic loading test was carried out once more to characterize the change in the material properties of the multilayer structure due to damage and repair. After the first experiment, the specimen was cut with a knife and repaired with the chitosan-based topohesive and silicone adhesive (fig. S13). The repaired specimen was used for cyclic loading test again, and the result shows that the electrical connection and properties under the external force were restored after the repair, supporting both the structural and functional reparability of the biomimetic structure after damage. The material characteristics were slightly changed after damage and repair, but the sensor performance was comparable to that of the intact specimen.

DNN for EIT
In this study, real-time EIT reconstruction was enabled by setting the model complexity to be moderately light. The training data were obtained by running finite element method simulations instead of directly applying pressure to the sensor (59) because various types of pressure can be applied in the simulation environment. We made

two mesh models: a nondeformed reference mesh model and a mesh model with deformation. These two mesh models calculated the degree of deformation (deformation map δ) and the corresponding measurement voltage (*v*) of the sensor. To accelerate the simulation, the measured voltage was obtained by assigning a conductivity value of zero to the mesh elements corresponding to the indented region instead of regenerating a deformed mesh model every time. Because the simulation data differ from the actual measurement data because of measurement noise and modeling errors, we tried to generalize the model by using a large amount of data and model normalization techniques.

For the machine learning pipeline, we performed latent learning (unsupervised) on the deformation map and EIT measurement vector, and then we obtained a projection between the two latent spaces (fig. S6). The length of the EIT measurement vector was 94, and it was encoded into 84 latent spaces through an autoencoder consisting of a fully connected network (FCN) with an exponential linear unit (ELU) function as an activation function. During autoencoder training, a dropout of 0.03 was added to prevent overfitting, and Gaussian noise was added to the input to make the trained model robust to measurement noise. Because the pattern itself used for measurements was already optimized (*60*), each measurement data had important information so that the number of neurons in the bottleneck layer could not be greatly reduced compared with the length of the measurement data.

The size of the deformation map was 48×48, and it was encoded into 128 latent spaces through a convolutional autoencoder (CAE). The CAE was also trained with Gaussian noise added to the input stage so that the trained model had a denoising property. The decoder part used an upsampling (nearest) + convolution operation instead of using a transposed convolution. The ELU function was used as an activation function in all layers.

Once the latent learning step was finished, the projection between the two latent spaces was obtained through supervised learning. The latent projections were FCNs with two hidden layers, with 84 inputs and 128 outputs. The number of neurons in the hidden layer was 256 and 256, and the activation function was the ELU function. To prevent overfitting, the encoder and decoder parts were not trained during latent projection training. The trained model could reconstruct the strain map in real time because of its light network structure. In addition, the reconstruction result was robust to measurement noise and showed relatively few artifacts compared with the image obtained through the conventional method (text S1).

CNN for touch modality classification

Touch modality classification was also performed in real time, similar to DNN-based EIT. The training data were obtained through experiments in which people applied dynamic tactile stimuli directly to the robotic skin. There were 10 people in the experiment, and each person applied four distinct stimuli to obtain 500 feature images for each stimulus. Measurement noise and ambient noise data were also collected for the same number as other stimuli and were labeled "none" to represent the absence of touch. Then, the collected dataset was augmented by adding Gaussian noise. To prevent overfitting, the dataset was randomly divided into a training set, a validation set, and a test set at a ratio of 8:1:1.

The size of each feature image was 89×41, corresponding to a time window with a duration of 0.5 s. To find the spatiotemporal pattern within a feature image, a CNN was used. The size of the first convolutional layer was $5 \times 5 \times 32$, and the image was not padded. The output of the first convolutional layer was input to the batch normalization and rectified linear (ReLU) activation layer. Then, it was downsized through the max-pooling layer. These operations (i.e., conv2D, batch normalization, ReLU, and MaxPool) were repeated once more with a different setting (fig. S7). Last, the output was flattened and progressed through the FCN layer with the softmax activation layer. The network was trained using an adaptive moment estimation (ADAM) optimizer with an initial learning rate of 0.0002, which drops by a factor of 0.1 every five epochs. The size of the mini batch was set to 64, and the cross-entropy loss was calculated every 50 iterations (training with mini batch). The training was set to be aborted if the loss did not decrease more than 20 times. The training was performed using a single GeForce RTX 3070 graphics processing unit. The trained network exhibited a 98.7% classification accuracy on the test set.

SUPPLEMENTARY MATERIALS

REFERENCES AND NOTES

1. M. Boniol, J. P. Verriest, R. Pedeux, J. F. Doré, Proportion of skin surface area of children and young adults from 2 to 18 years old. *J. Invest. Dermatol.* **128**, 461–464 (2008).
2. J. M. Loomis, S. J. Lederman, Tactual perception. *Handbook Percept. Hum. Perform.* **2**, 2 (1986).
3. V. G. Macefield, I. Birznieks, Cutaneous mechanoreceptors, functional behavior, in *Encyclopedia of Neuroscience*, M. D. Binder, N. Hirokawa, U. Windhorst, Eds. (Springer, 2009).
4. J. M. Loomis, C. C. Collins, Sensitivity to shifts of a point stimulus: An instance of tactile hyperacuity. *Percept. Psychophys.* **24**, 487–492 (1978).
5. E. P. Gardner, J. H. Martin, Coding of sensory information, in *Principles of Neural Science*, E. R. Kandel, J. H. Schwartz, T. M. Jessell, Eds. (McGraw-Hill, ed. 4, 2000), pp. 411–429.
6. G. Cheng, E. Dean-Leon, F. Bergner, J. R. G. Olvera, Q. Leboutet, P. Mittendorfer, A comprehensive realization of robot skin: Sensors, sensing, control, and applications. *Proc. IEEE* **107**, 2034–2051 (2019).
7. F. Nori, S. Traversaro, J. Eljaik, F. Romano, A. del Prete, D. Pucci, iCub whole-body control through force regulation on rigid non-coplanar contacts. *Front. Robot. AI* **2**, 1–18 (2015).
8. L. E. Osborn, A. Dragomir, J. L. Betthauser, C. L. Hunt, H. H. Nguyen, R. R. Kaliki, N. V. Thakor, Prosthesis with neuromorphic multilayered e-dermis perceives touch and pain. *Sci. Robot.* **3**, 10.1126/scirobotics.aat3818 (2018).
9. A. Chortos, J. Liu, Z. Bao, Pursuing prosthetic electronic skin. *Nat. Mater.* **15**, 937–950 (2016).
10. D. Silvera-Tawil, D. Rye, M. Soleimani, M. Velonaki, Electrical impedance tomography for artificial sensitive robotic skin: A review. *IEEE Sens. J.* **15**, 2001–2016 (2015).
11. T. Mukai, M. Onishi, T. Odashima, S. Hirano, Z. Luo, Development of the tactile sensor system of a human-interactive robot "RI-MAN". *IEEE Trans. Robot.* **24**, 505–512 (2008).
12. C. M. Boutry, M. Negre, M. Jorda, O. Vardoulis, A. Chortos, O. Khatib, Z. Bao, A hierarchically patterned, bioinspired e-skin able to detect the direction of applied pressure for robotics. *Sci. Robot.* **3**, eaau6914 (2018).
13. T. Someya, T. Sekitani, S. Iba, Y. Kato, H. Kawaguchi, T. Sakurai, A large-area, flexible pressure sensor matrix with organic field-effect transistors for artificial skin applications. *Proc. Natl. Acad. Sci. U.S.A.* **101**, 9966–9970 (2004).
14. S. M. Won, H. Wang, B. H. Kim, K. Lee, H. Jang, K. Kwon, M. Han, K. E. Crawford, H. Li, Y. Lee, X. Yuan, S. B. Kim, Y. S. Oh, W. J. Jang, J. Y. Lee, S. Han, J. Kim, X. Wang, Z. Xie, Y. Zhang, Y. Huang, J. A. Rogers, Multimodal sensing with a three-dimensional piezoresistive structure. *ACS Nano* **13**, 10972–10979 (2019).
15. A. Schmitz, P. Maiolino, M. Maggiali, L. Natale, G. Cannata, G. Metta, Methods and technologies for the implementation of large-scale robot tactile sensors. *IEEE Trans. Robot.* **27**, 389–400 (2011).
16. P. Mittendorfer, G. Cheng, Humanoid multimodal tactile-sensing modules. *IEEE Trans. Robot.* **27**, 401–410 (2011).
17. W. W. Lee, Y. J. Tan, H. Yao, S. Li, H. H. See, M. Hon, K. A. Ng, B. Xiong, J. S. Ho, B. C. K. Tee, A neuro-inspired artificial peripheral nervous system for scalable electronic skins. *Sci. Robot.* **4**, eaax2198 (2019).

18. L. van Duong, V. A. Ho, Large-scale vision-based tactile sensing for robot links: Design, modeling, and evaluation. *IEEE Trans. Robot.* **37**, 390–403 (2021).

19. D. Hughes, N. Correll, Texture recognition and localization in amorphous robotic skin. *Bioinspir. Biomim.* **10**, 055002 (2015).

20. K. Park, H. Park, H. Lee, S. Park, J. Kim, An ERT-based robotic skin with sparsely distributed electrodes: Structure, fabrication, and DNN-based signal processing, in *2020 IEEE International Conference on Robotics and Automation (ICRA)* (IEEE, 2020), pp. 1617–1624.

21. H. Lee, K. Park, J. Kim, K. J. Kuchenbecker, Piezoresistive textile layer and distributed electrode structure for soft whole-body tactile skin. *Smart Mater. Struct.* **30**, 085036 (2021).

22. C. Gervaise, S. Vallez, C. Ioana, Y. Stephan, Y. Simard, Passive acoustic tomography: New concepts and applications using marine mammals: A review. *J. Marine Biol. Assoc. United Kingdom* **87**, 5–10 (2007).

23. H. Lee, K. Park, Y. Kim, J. Kim, Durable and repairable soft tactile skin for physical human robot interaction, in *Proceedings of the Companion of the 2017 ACM/IEEE International Conference on Human-Robot Interaction* (ACM, 2017), pp. 183–184.

24. Y. Hara, Y. Masuda, T. Hirao, N. Yoshikawa, The relationship between the Young's modulus of the stratum corneum and age: A pilot study. *Skin Res. Technol.* **19**, 339–345 (2013).

25. M. Geerligs, *Skin Layer Mechanics* (TU Eindhoven, 2010).

26. R. S. Dahiya, G. Metta, M. Valle, G. Sandini, Tactile sensing—From humans to humanoids. *IEEE Trans. Robot.* **26**, 10.1109/TRO.2009.2033627 (2010).

27. G. J. Gerling, G. W. Thomas, The role of fingertip microstructures on tactile edge perception, in *Proceedings of the 1st Joint Eurohaptics Conference and Symposium on Haptic Interfaces for Virtual Environment and Teleoperator Systems* (World Haptics Conference, WHC, 2005), pp. 63–72.

28. C. Molnar, J. Gair, C. Rye, Y. Avissar, V. Jurukovski, S. Fowler, R. Wise, R. Roush, J. Choi, J. DeSaix, M. Wise, M. Nakano, *Concepts of Biology: 1st Canadian Edition* (BCcampus, 2015).

29. R. Schleip, Fascia as a sensory organ—A target of myofascial manipulation, in *Dynamic Body: Exploring Form, Expanding Function* (Freedom From Pain Institute, 2011), pp. 137–164.

30. M. Kumka, J. Bonar, Fascia: A morphological description and classification system based on a literature review. *J. Can Chiropr. Assoc.* **56**, 179–191 (2012).

31. H. Yuk, T. Zhang, G. A. Parada, X. Liu, X. Zhao, Skin-inspired hydrogel–elastomer hybrids with robust interfaces and functional microstructures. *Nat. Commun.* **7**, 12028 (2016).

32. J. J. Park, S. Haddadin, J. B. Song, A. Albu-Schäffer, Designing optimally safe robot surface properties for minimizing the stress characteristics of Human-Robot collisions, in *Proceedings of the IEEE International Conference on Robotics and Automation* (IEEE, 2011), pp. 5413–5420.

33. P. Le Floch, X. Yao, Q. Liu, Z. Wang, G. Nian, Y. Sun, L. Jia, Z. Suo, Wearable and washable conductors for active textiles. *ACS Appl. Mater. Interfaces* **9**, 25542–25552 (2017).

34. B. Chen, J. J. Lu, C. H. Yang, J. H. Yang, J. Zhou, Y. M. Chen, Z. Suo, Highly stretchable and transparent ionogels as nonvolatile conductors for dielectric elastomer transducers. *ACS Appl. Mater. Interfaces* **6**, 7840–7845 (2014).

35. C. C. Kim, H. H. Lee, K. H. Oh, J. Y. Sun, Highly stretchable, transparent ionic touch panel. *Science* **353**, 682–687 (2016).

36. D. Silvera-Tawil, D. Rye, M. Velonaki, Artificial skin and tactile sensing for socially interactive robots: A review. *Robot. Autonomous Syst.* **63**, 230–243 (2015).

37. J. Yang, J. Steck, R. Bai, Z. Suo, Topological adhesion II. Stretchable adhesion. *Extreme Mech Lett.* **40**, 100891 (2020).

38. Y. Gao, K. Wu, Z. Suo, Photodetachable adhesion. *Adv. Mater.* **31**, 1806948 (2019).

39. L. Jin, A. Chortos, F. Lian, E. Pop, C. Linder, Z. Bao, W. Cai, Microstructural origin of resistance—Strain hysteresis in carbon nanotube thin film conductors. *Proc. Natl. Acad. Sci.* **115**, 1986–1991 (2018).

40. R. J. Halter, A. Hartov, K. D. Paulsen, A broadband high-frequency electrical impedance tomography system for breast imaging. *IEEE Trans. Biomed. Eng.* **55**, 650–659 (2008).

41. A. Borsic, B. M. Graham, A. Adler, W. R. B. Lionheart, In vivo impedance imaging with total variation regularization. *IEEE Trans. Med. Imaging* **29**, 44–54 (2010).

42. G. Bouchette, P. Church, J. E. McFee, A. Adler, Imaging of compact objects buried in underwater sediments using electrical impedance tomography. *IEEE Trans. Geosci. Remote Sens.* **52**, 1407–1417 (2014).

43. Y. Wu, D. Jiang, X. Liu, R. Bayford, A. Demosthenous, A human-machine interface using electrical impedance tomography for hand prosthesis control. *IEEE Trans. Biomed. Circuits Syst.* **12**, 1322–1333 (2018).

44. Y. Zhang, R. Xiao, C. Harrison, Advancing hand gesture recognition with high resolution electrical impedance tomography, in *Proceedings of the 29th Annual Symposium on User Interface Software and Technology (UIST 2016)* (ACM, 2016), pp. 843–850.

45. D. R. Merrill, M. Bikson, J. G. R. Jefferys, Electrical stimulation of excitable tissue: Design of efficacious and safe protocols. *J. Neurosci. Methods* **141**, 171–198 (2005).

46. S. Liu, J. Jia, Y. D. Zhang, Y. Yang, Image reconstruction in electrical impedance tomography based on structure-aware sparse bayesian learning. *IEEE Trans. Med. Imaging* **37**, 2090–2102 (2018).

47. M. Cheney, D. Isaacson, J. C. Newell, S. Simske, J. Goble, NOSER: An algorithm for solving the inverse conductivity problem. *Int. J. Imaging Syst. Technol.* **2**, 66–75 (1990).

48. H. Park, K. Park, S. Mo, J. Kim, Deep neural network based electrical impedance tomographic sensing methodology for large-area robotic tactile sensing. *IEEE Trans. Robot.* **37**, 1570–1583 (2021).

49. Y. Narang, B. Sundaralingam, M. Macklin, A. Mousavian, D. Fox, Sim-to-Real for robotic tactile sensing via physics-based simulation and learned latent projections, in *Proceedings of the IEEE International Conference on Robotics and Automation (ICRA)* (IEEE, 2021).

50. J. Yang, R. Bai, Z. Suo, Topological adhesion of wet materials. *Adv. Mater.* **30**, 1800671 (2018).

51. M. Teyssier, G. Bailly, C. Pelachaud, E. Lecolinet, A. Conn, A. Roudaut, Skin-on interfaces: A bio-driven approach for artificial skin design to cover interactive devices, in *Proceedings of the 32nd Annual ACM Symposium on User Interface Software and Technology (UIST 2019)* (ACM, 2019), pp. 307–322.

52. H. Lee, D. Kwon, H. Cho, I. Park, J. Kim, Soft nanocomposite based multi-point, multi-directional strain mapping sensor using anisotropic electrical impedance tomography. *Sci. Rep.* **7**, 39837 (2017).

53. I. M. Van Meerbeek, C. M. De Sa, R. F. Shepherd, Soft optoelectronic sensory foams with proprioception. *Sci. Robot.* **3**, eaau2489 (2018).

54. Y. Yan, Z. Hu, Z. Yang, W. Yuan, C. Song, J. Pan, Y. Shen, Soft magnetic skin for super-resolution tactile sensing with force self-decoupling. *Sci. Robot.* **6**, abc8801 (2021).

55. Z. Lei, Q. Wang, S. Sun, W. Zhu, P. Wu, A bioinspired mineral hydrogel as a self-healable, mechanically adaptable ionic skin for highly sensitive pressure sensing. *Adv. Mater.* **29**, 1700321 (2017).

56. Z. Lei, P. Wu, A supramolecular biomimetic skin combining a wide spectrum of mechanical properties and multiple sensory capabilities. *Nat. Commun.* **9**, 1134 (2018).

57. H. Yuk, T. Zhang, S. Lin, G. A. Parada, X. Zhao, Tough bonding of hydrogels to diverse non-porous surfaces. *Nat. Mater.* **15**, 190–196 (2016).

58. Y. Yu, H. Yuk, G. A. Parada, Y. Wu, X. Liu, C. S. Nabzdyk, K. Youcef-Toumi, J. Zang, X. Zhao, Multifunctional "hydrogel skins" on diverse polymers with arbitrary shapes. *Adv. Mater.* **31**, e1807101 (2019).

59. A. Adler, W. R. B. Lionheart, Uses and abuses of EIDORS: An extensible software base for EIT. *Physiol. Meas.* **27**, S25–S42 (2006).

60. K. Park, H. Lee, K. J. Kuchenbecker, J. Kim, Adaptive optimal measurement algorithm for ERT-based large-area tactile sensors. *IEEE/ASME Trans. Mechatronics* **4435**, 304–314 (2021).

61. D. S. Holder, *Electrical Impedance Tomography: Methods, History and Applications* (CRC Press, 2004).

62. R. Zekavat, R. M. Buehrer, *Handbook of Position Location: Theory, Practice and Advances* (John Wiley & Sons, 2011), vol. 27.

63. N. F. Lepora, U. Martinez-Hernandez, M. Evans, L. Natale, G. Metta, T. J. Prescott, Tactile superresolution and biomimetic hyperacuity. *IEEE Trans. Robot.* **31**, 605–618 (2015).

64. S. Lederman, R. Klatzky, Haptic perception: A tutorial. *Atten. Percept. Psychophys.* **71**, 1439–1459 (2009).

Science Robotics

A biomimetic elastomeric robot skin using electrical impedance and acoustic tomography for tactile sensing

K. ParkH. YukM. YangJ. ChoH. LeeJ. Kim

View the article online
Permissions
https://www.science.org/help/reprints-and-permissions

Use of this article is subject to the Terms of service

Science Robotics

AAAS

Supplementary Materials for

A biomimetic elastomeric robot skin using electrical impedance and acoustic tomography for tactile sensing

K. Park *et al.*

Corresponding author: J. Kim, jungkim@kaist.ac.kr

The PDF file includes:

Other Supplementary Material for this manuscript includes the following:

Text S1. Reconstruction of strain using electrical impedance tomography (EIT)

Electrical impedance tomography (EIT) is a reconstruction method developed to capture the impedance distribution inside a conductive medium using electrodes on the surface (*61*). The EIT technique measures the voltages from the electrodes and converts the voltages to a conductivity distribution of the medium. The former process is a forward problem, and the latter is an inverse problem. The forward EIT problem aims to find the voltage ϕ on the boundary $\partial\Omega$ when the conductivity distribution σ in a conductive domain Ω is given. The continuum version of Kirchhoff's law describes the following relationships between the potential ϕ and the conductivity distribution σ in the region Ω and the boundary condition on $\partial\Omega$.

$$\nabla \cdot (\sigma \nabla \phi) = 0 \quad \text{in } \Omega$$
$$j = \sigma \nabla \phi \cdot \mathbf{n} \quad \text{in } \partial\Omega$$

where j denotes the current density and $\mathbf{n}$ is the unit normal vector on $\partial\Omega$. This is a Dirichlet-Neumann boundary value problem for the Laplacian elliptical partial difference equation, and can be solved with the finite element method. The inverse problem reconstructs the conductivity distribution ($\boldsymbol{\sigma}$) from a set of voltage measurements ($\mathbf{V}$). This process is generally ill-posed and nonlinear; thus, linearization is widely used for fast computation.

$$\Delta\mathbf{V} \approx \mathbf{J}\Delta\boldsymbol{\sigma} + \mathbf{w}$$

where $\boldsymbol{\sigma}$ is the conductivity distribution (defined in mesh elements), $\mathbf{J}$ is the Jacobian matrix calculated from the initial conductivity with a given pattern, and $\mathbf{w}$ is measurement noise. The linearized inverse problem can be solved by minimizing the square of the L_2-norm of the estimation error. As a result, we can estimate the conductivity change with the pseudoinverse of the Jacobian matrix as follows:

$$\Delta\boldsymbol{\sigma} = (\mathbf{J}^{\mathrm{T}}\mathbf{J})^{-1}\mathbf{J}^{\mathrm{T}}\Delta\mathbf{V}$$

However, calculating the pseudoinverse directly from the Jacobian $\mathbf{J}$ is unstable if the rank of $\mathbf{J}$ is smaller than the length of the vector $\boldsymbol{\sigma}$. Hence, regularization methods are used to stabilize the solution.

$$\underset{\Delta\boldsymbol{\sigma}}{\mathrm{argmin}}\{\|\mathbf{J}\Delta\boldsymbol{\sigma} - \Delta\mathbf{V}\|_2^2 + \|\boldsymbol{\Gamma}\Delta\boldsymbol{\sigma}\|_2^2\}$$

where $\boldsymbol{\Gamma}$ is the Laplacian-type regularization matrix that extracts the high-spatial-frequency components from the conductivity distribution. We can derive the mapping matrix between $\Delta\boldsymbol{\sigma}$ and $\Delta\mathbf{V}$ by the above minimization problem.

$$\Delta\boldsymbol{\sigma} = (\mathbf{J}^{\mathrm{T}}\mathbf{J} + \alpha^2\boldsymbol{\Gamma}^{\mathrm{T}}\boldsymbol{\Gamma})^{-1}\mathbf{J}^{\mathrm{T}}\Delta\mathbf{V}$$

where α is a scalar hyperparameter that adjusts the strength of the regularization. This method is one of the most straightforward ways to reconstruct the deformation map from measurement data, but the reconstruction results are often blurred or distorted. The iterative methods would exhibit better reconstruction results, but their uses in tactile sensors are limited due to the heavy computational load that limits the real-time reconstruction. Thus, iterative methods are not practical for use in robotic skin. To resolve this trade-off between the quality and speed of reconstruction, a deep neural network-based EIT reconstruction has been introduced to achieve image quality and speed simultaneously. The neural network could deal with the ill-posedness and nonlinearity of the EIT inverse problem effectively, demonstrating an accurate yet fast reconstruction.

Text S2. Localization of touch using passive acoustic tomography (PAT)

The developed robotic skin can detect dynamic tactile stimuli (e.g., pat, tickle, stroke) by using microphones that measure a vibration due to touch. These vibrations are propagated to other parts of the robotic skin, and their amplitude decays over the distance. This characteristic indicates that the microphones have a large and overlapping receptive field. Thus, the vibration source can be localized based on the energy of the signal obtained from each microphone and the characteristics of the receptive field (i.e., the energy decay model). This technique has been widely used for the positioning of people and objects (*62*), and it is often called passive acoustic tomography (PAT) depending on the application (*22*).

The developed robotic skin is made of hydrogel-elastomer hybrids, and the vibration is propagated through this multilayer structure. Since each layer shows nonlinear and viscoelastic material properties, it is not easy to obtain an analytical model for energy decay. These characteristics also make simulation difficult, and it cannot be guaranteed that the simulation results and the actual sensor characteristics match well. In addition, each microphone has different characteristics (e.g., sensitivity, receptive field) and needs to be calibrated manually. Thus, we conducted an experiment to apply vibration to the surface of robotic skin and obtained the receptive field of each microphone using the experimental data. Here, we modeled each receptive field of the ith microphone as

$$I_i \approx I_0 \left(\frac{a_i}{r_i^2 + b_i} \right)$$

where I_0 is the intensity at the source, r_i is the distance between the ith microphone and the vibration source, and a_i and b_i are fitting parameters. If we assume that there is only a single vibration source, then I_0 is equal for every microphone. Therefore, for any i and j,

$$I_0 = I_i \left(\frac{(\mathbb{x} - \mathbb{x}_i)^2 + b_i}{a_i} \right) = I_j \left(\frac{\left(\mathbb{x} - \mathbb{x}_j\right)^2 + b_j}{a_j} \right)$$

where $\mathbb{x}$ is the position of the source and $\mathbb{x}_i$ is the position of the ith microphone. However, measured data hardly meet this equation due to noise and modeling error. If there are N microphones, then N-1 independent equations of error can be derived as below.

$$\varepsilon_{i,j}(\mathbb{x}) = \hat{I}_i \left(\frac{(\mathbb{x} - \mathbb{x}_i)^2 + b_i}{a_i} \right) - \hat{I}_j \left(\frac{\left(\mathbb{x} - \mathbb{x}_j\right)^2 + b_j}{a_j} \right)$$

where $\hat{I}_i$ is the measured intensity of the signal from the ith microphone. Assuming the kth microphone has the largest intensity, we can define a loss function L as a sum of error ε values, as shown below.

$$L = \sum_{i \neq k} \varepsilon_{k,i}^2(\mathbb{x}) = \sum_{i \neq k} \left\{ \hat{I}_i \left(\frac{(\mathbb{x} - \mathbb{x}_i)^2 + b_i}{a_i} \right) - \hat{I}_j \left(\frac{\left(\mathbb{x} - \mathbb{x}_j\right)^2 + b_j}{a_j} \right) \right\}^2$$

Then, the location of the vibration source is determined by finding the value of $\tilde{\mathbb{x}}$ that minimizes the loss function L.

$$\tilde{\mathbb{x}} = \underset{\mathbb{x}}{\operatorname{argmin}} L = \underset{\mathbb{x}}{\operatorname{argmin}} \sum_{i \neq k} \left\{ \hat{I}_i \left(\frac{(\mathbb{x} - \mathbb{x}_i)^2 + b_i}{a_i} \right) - \hat{I}_j \left(\frac{\left(\mathbb{x} - \mathbb{x}_j\right)^2 + b_j}{a_j} \right) \right\}^2$$

Text S3. Measurement device for EIT and PAT

A field-programmable gate array (FPGA)-based data acquisition system (myRIO-1900, National Instrument, USA) was used to obtain both voltage measurements for the EIT and audio signals for the PAT (Fig. S10). To use EIT, it is necessary to select an electrode for current injection and voltage measurement, and several measurements are required to reconstruct a single EIT image. Therefore, voltage conversion and electrode switching must be conducted at fast and accurate timing to achieve a fast frame rate. Additionally, PAT requires receiving signals from multiple microphones simultaneously. To achieve these requirements, we utilized an FPGA-based measurement system (Fig. S10). The developed system had several analog/digital channels, and 10 analog inputs and 22 digital outputs were used for voltage measurement and multiplexing. The EIT utilized its 20 digital outputs to control each of the four 32:1 multiplexers and to inject current and measure voltage to the sensor. A fixed voltage source was used for current injection, and a variable resistor was connected in series to the channel through which the current was injected. The measured value was corrected by calculating the actual current applied to the sensor by measuring the voltage across this resistor. The PAT utilized eight analog inputs to measure dynamic tactile signals from eight microphones. To increase the number of available microphones, eight multiplexers (4:1 multiplexing) were controlled with the same digital signal (2 channels) so that up to 32 microphones could be utilized. The circuits for the operation of EIT and PAT were manufactured separately and stacked on the data acquisition system (DAQ, myRIO-1900) for simultaneous operation. To suppress the reactance of the hydrogel, a square wave (-1 V to 1 V) with a frequency of 40 kHz was injected into the sensor instead of DC current, and the measurement was also performed according to the current direction. Since the measurement value is very noisy, the previous measurement data were loaded for each measurement and filtered with a first-order LPF with a cut-off frequency of 45 Hz. In the FPGA chip of the DAQ, the filtered value was buffered to the host at a rate of 60 Hz and transmitted through the first-in, first-out (FIFO) function. Simultaneously, with the EIT measurement, the microphone signal for the PAT was also measured in parallel. The sampling time of the 8 microphones was 25 microseconds, and 25 acoustic signals took approximately 100 microseconds.

Text S4. Comparison between different electrode arrangements

The intrinsic characteristics of the developed sensor is evaluated by analyzing the result of the forward problem (FEM simulation) First, we defined the sensitivity as the L_2 norm of the changes in the output vector due to a unit deformation (a bell-shaped surface with a depth of 2.5 mm and a standard deviation of 7.5 mm). The shape of the unit deformation was determined as a bell-shaped surface considering the actual deformation of the sensor during the indentation with a hemispherical tip (Fig. S1).

Consider a forward model in which the numbers of electrodes and mesh elements are L and M, respectively. Then, the conductivity distribution is expressed as a vector $\boldsymbol{\sigma} \in \mathbb{R}^{M \times 1}$, and the electrical behavior of the sensor model can be represented by using a transfer impedance matrix $\mathbf{S}(\boldsymbol{\sigma}) \in \mathbb{R}^{L \times L}$:

$$\boldsymbol{\varphi}(\cdot \ ; \boldsymbol{\sigma}, \mathbf{p}) = \mathbf{S}(\boldsymbol{\sigma}) \cdot \mathbf{p}$$

where $\mathbf{p} \in \mathbb{R}^{L \times 1}$ is the current injected through the electrodes and $\boldsymbol{\varphi} \in \mathbb{R}^{L \times 1}$ is the resulting potential on the electrodes. If the conductivity distribution changes, then the transfer impedance matrix $\mathbf{S}$ becomes

$$\mathbf{S}(\boldsymbol{\sigma} + \Delta\boldsymbol{\sigma}) = \mathbf{S}(\boldsymbol{\sigma}) + \Delta\mathbf{S}$$

Then, the change in the resulting potential is determined as follows:

$$\Delta v = \mathbf{m}^{\mathbf{T}} \cdot \Delta\mathbf{S} \cdot \mathbf{p}$$

where $\mathbf{m} \in \mathbb{R}^{L \times 1}$ is the measurement vector. Above equation can be rewritten by using a Kronecker product as

$$\Delta v = (\mathbf{p}^{\mathbf{T}} \otimes \mathbf{m}^{\mathbf{T}}) \cdot \Delta\mathbf{s} = \mathbf{g} \cdot \Delta\mathbf{s}$$

where $\Delta\mathbf{s}$ is a vectorization of $\Delta\mathbf{S}$. The vector $\mathbf{g} \in \mathbb{R}^{1 \times L^2}$ is defined to combine the vectors $\mathbf{m}$ and $\mathbf{p}$. This equation can be extended by concatenating the row vectors $\mathbf{g}$ to form a matrix G, which represent the given EIT electrode pattern of length N.

$$\Delta\mathbf{v} = \mathbf{G} \cdot \Delta\mathbf{s}, \qquad \text{where} \ \ \mathbf{G} = \begin{pmatrix} \mathbf{g_1} \\ \vdots \\ \mathbf{g_N} \end{pmatrix}$$

Finally, the sensitivity map $\boldsymbol{\Theta} \in \mathbb{R}^{48 \times 48}$ can be defined as below.

$$\boldsymbol{\Theta}(i,j) = \left\| \Delta\mathbf{v}_{(i,j)} \right\|_2, \qquad \text{where} \quad \Delta\mathbf{v}_{(i,j)} = \mathbf{G} \cdot \left\{ \mathbf{s}\left(\boldsymbol{\sigma}_0 + \Delta\boldsymbol{\sigma}_{(i,j)}\right) - \mathbf{s}(\boldsymbol{\sigma}_0) \right\} = \mathbf{G} \cdot \Delta\mathbf{s}_{(i,j)}$$

The sensor surface was discretized into 2304 regions (48×48 grid) and the unit deformation is defined for each region. The vector $\Delta\boldsymbol{\sigma}_{(i,j)}$ represents the change in conductivity distribution, and it is simulated by assigning zero conductivity value to the mesh elements corresponding to the indented portion of the sensor (Fig. S11A). Next, we

obtained the changes in output voltage $\Delta\mathbf{v}_{(i,j)}$ by solving the forward problem (FEM). Finally, we could obtain the sensitivity map by performing these simulations for all regions of the sensor (48-by-48 grid). We obtained sensitivity maps from two mesh models with different electrode arrangements (Fig. S11B-C). This result shows that our design has a sensitivity map with uniform and high values. In particular, the conventional design has a sensitivity below our design's minimum sensitivity in 33% of its sensing area. It means that the conventional design has a 'blind spot' in the center region. In this case, we cannot obtain a significant level of change in output unless a high-contrast conductivity perturbation (or deep deformation) occurs over a large area.

Second, we evaluate the spatial acuity of the robotic skin by introducing a concept of virtual taxel. In general, the spatial resolution of the pressure sensor is determined by the distance between the taxels that exist individually. However, the tactile acuity actually depends on a combination of factors, including the taxels' density and spatial layout, and the size/shape of the receptive field, coupled with utilizing active and probabilistic methods for perception (*63*). It means that we have to investigate how the taxels (or sensor signals) respond to tactile stimuli.

Inspired by this perspective, we quantified the spatial acuity based on the similarity of the output change due to local deformation for each location of the sensor surface. The sensor surface was divided into 2304 regions, and local deformation was simulated in each location to obtain the change in sensor outputs ($\Delta\mathbf{v}$) as below.

$$\Delta\mathbf{v}_{(i,j)} = \mathbf{G} \cdot \Delta\mathbf{s}_{(i,j)}$$

Here, we grouped regions that produce similar output pattern by applying *k*-means clustering algorithm to the vectors $\Delta\mathbf{v}_{(i,j)}$. Then, we calculated the cosine similarity between the centroid of each cluster $(\Delta\boldsymbol{\mu}_k)$ and all vectors $(\Delta\mathbf{v}_{(i,j)})$.

$$S(\Delta\boldsymbol{\mu}_k, \Delta\mathbf{v}_{(i,j)}) = \frac{\Delta\boldsymbol{\mu}_k \cdot \Delta\mathbf{v}_{(i,j)}}{\|\Delta\boldsymbol{\mu}_k\|\|\Delta\mathbf{v}_{(i,j)}\|}$$

Next, we defined a similarity surface for each cluster as below.

$$S_k(i,j) = S(\Delta\boldsymbol{\mu}_k, \Delta\mathbf{v}_{(i,j)})$$

Then, these surfaces are a visual representation of how similar each position generates an output vector to each other. If the similarity surface is spread out, each position produces an output vector that is similar to the others. Conversely, if the similarity surface is concentrated at each location, it means that each location produces an output vector that is distinguishable from the others. We obtained similarity surfaces from both models through *k*-means clustering with a hyperparameter of 90. Examples of the similarity surfaces shows that our design has less spread similarity surface, implying that the grid-like electrode arrangement has much better spatial acuity than the conventional design (Fig. S11D).

For quantification, we defined virtual taxels by quantizing the similarity surfaces with a threshold of 0.7 (Fig. S11E-F). The results present that our design has much sharp spatial acuity than the conventional design; in our design, the virtual taxels were evenly arranged, and the average area of the virtual taxels is 12.6 cm^2 (Std. = 1.4 cm^2). This is

approximately 3.15 % of the sensing area. Since the adjacent taxels overlapped each other appropriately, the robotic skin could achieve tactile super-resolution through tomographic imaging (Fig. S8). As a result, the single-point contact (deep pressure) could be localized with an error or about 4.2 mm, and the two-point discrimination threshold is at least 41 mm (average diameter of the virtual taxels); this level of tactile spatial acuity is better than the back or thigh of humans (*64*).

On the other hand, in the case of the conventional design, the virtual taxels were very large and substantially overlapped. In particular, the virtual taxels overlapped seriously at the central region, and their average size is 30.5 cm^2 (Std. = 27.3 cm^2, Max. = 112 cm^2). It means that every location of the sensor changes an output vector in a similar pattern, resulting in a8 compromised tactile acuity. Although it would still be possible to localize single-point stimuli even with conventional designs, it will be fundamentally difficult to discriminate multi-point contacts, especially closely located tactile stimuli.
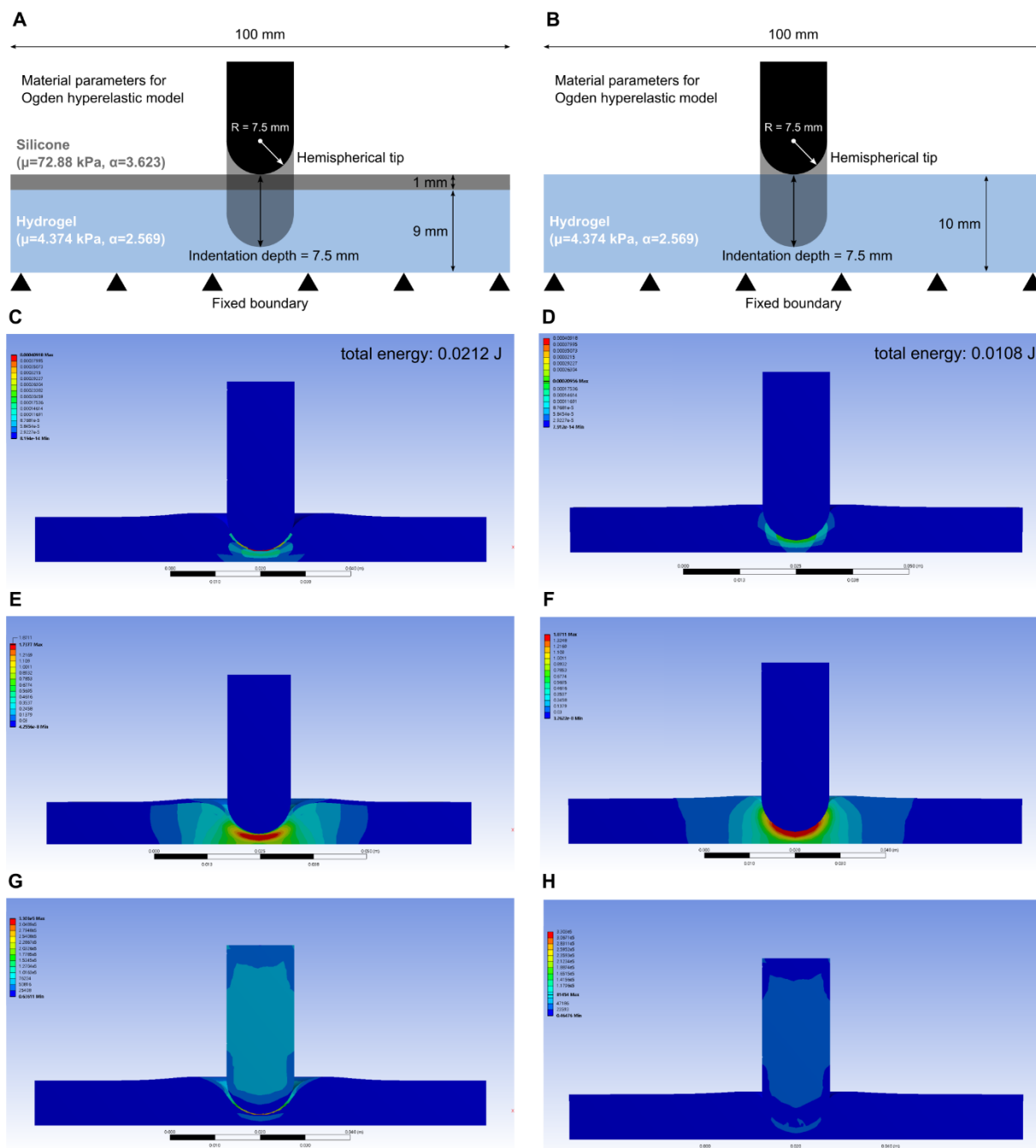
Fig. S1. Simulation of deformation of the multilayer structure by indentation. (**A-B**) Simulation setup and material properties for the hydrogel-elastomer hybrid and a single layer of hydrogel; (**C-D**) Strain energy during to the indentation. The resulting strain energy doubled due to the elastomeric skin; (**E-F**) Equivalent elastic strain due to the indentation. The simulation results show that the thin elastomeric skin spreads the pressure over a large area; and (**G-H**) Equivalent (von-mises) stress. The stress is concentrated on the elastomeric skin due to its relatively high modulus.
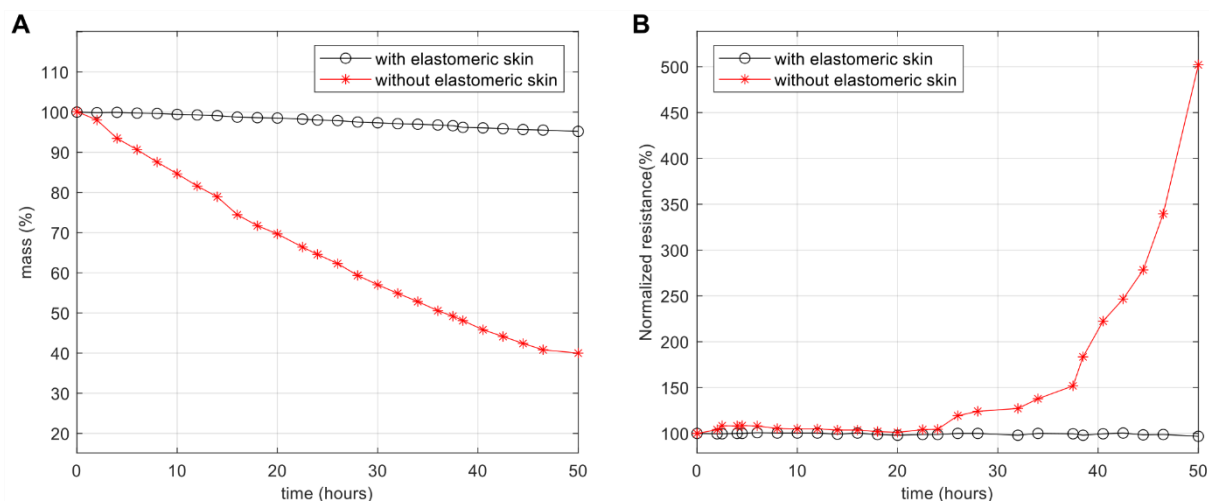
Fig. S2. Anti-dehydration effect of multi-layer structure. (**A**) The elastomeric skin effectively prevents moisture loss of hydrogel; (**B**) The elastomeric skin also prevents resistance changes due to moisture loss.
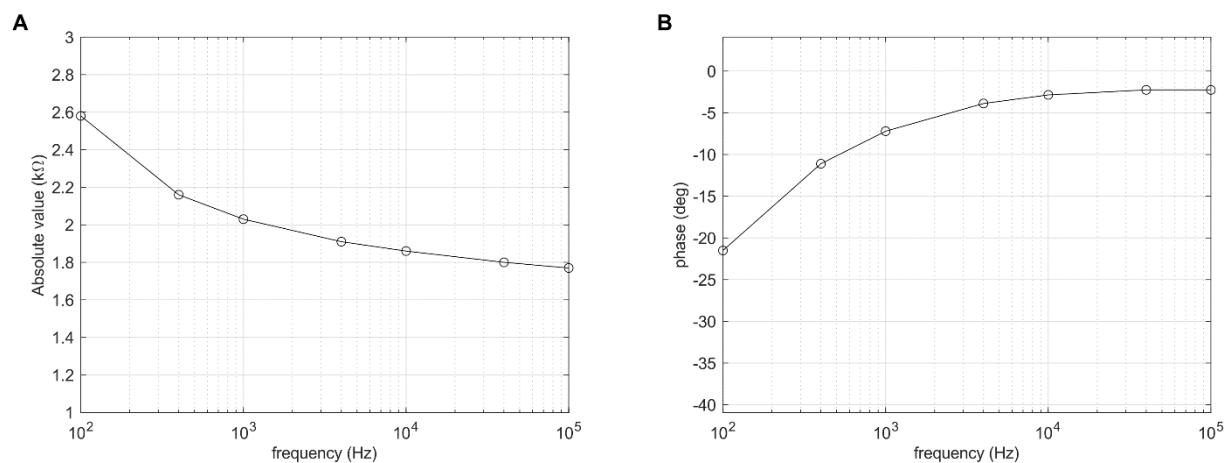

Fig. S3. Impedance of the polyacrylamide-alginate hydrogel. (**A**) Absolute value of the impedance; and (**B**) Phase of the impedance. The result shows that the phase decreases as the frequency of the excitation voltage increases.
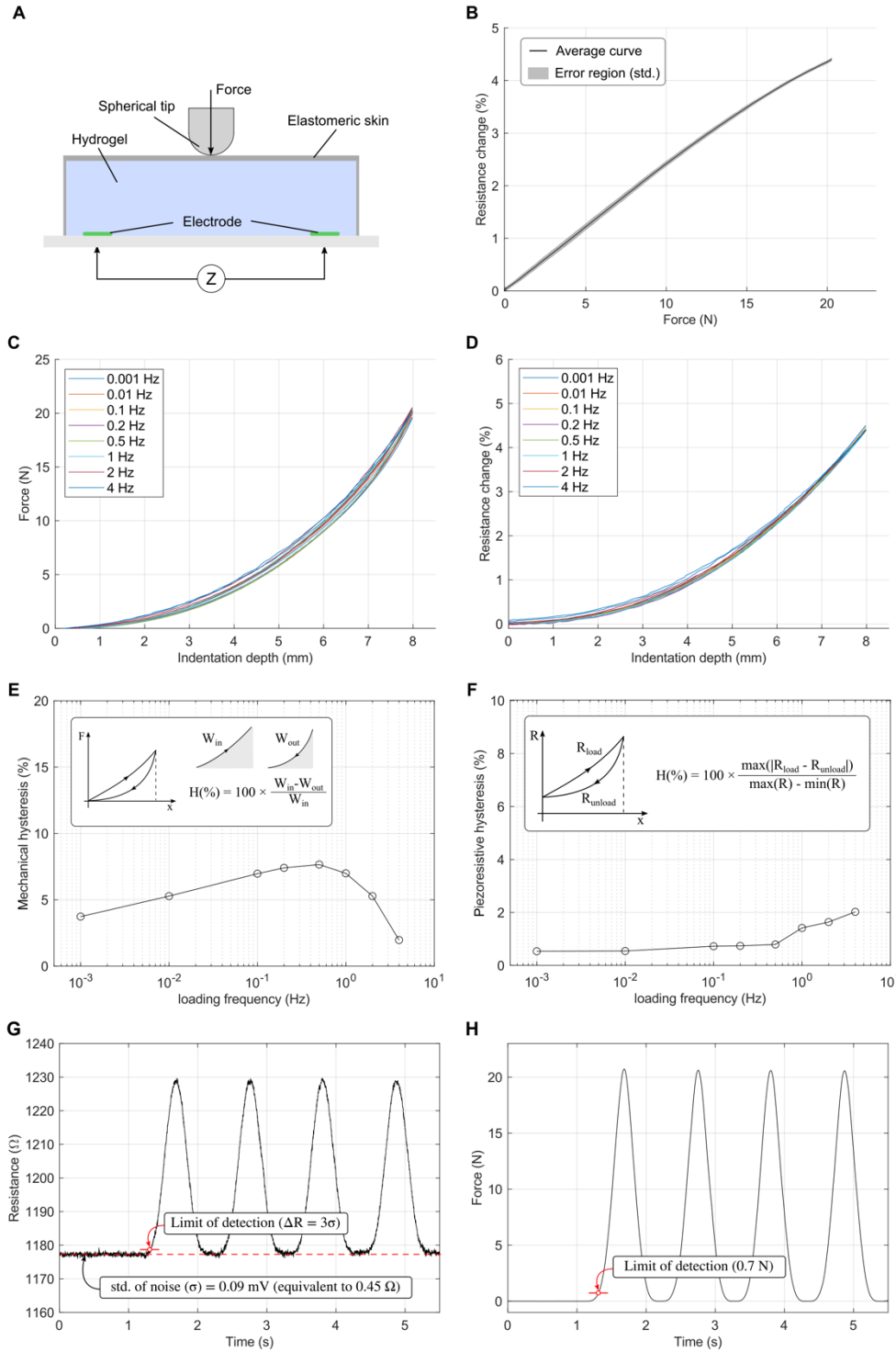
Fig. S4. Mechanical and piezoresistive characteristics of the hydrogel-elastomer hybrid. (**A**) Specimen for the cyclic loading test. The specimen was prepared with dimensions of 40 mm in width, 55 mm in length, and 10 mm in thickness. The electrodes had a radius of 3 mm and were spaced by 43 mm from each other; (**B**) Relationship between force and normalized resistance change; (**C**) Relationship between indentation depth and force; (**D**) Relationship between indentation depth and normalized resistance change; (**E**) Mechanical hysteresis; and (**F**) Piezoresistive hysteresis. The mechanical hysteresis is defined as the ratio between the input and loss of the work during the loading cycle. The piezoresistive hysteresis is defined as the maximum difference between the loading and unloading curves (resistance) divided by the maximum resistance difference during the loading. (**G**) Measured resistance during the experiment. The standard deviation of the measurement noise was 0.45 Ω approximately; (**H**) Applied force during the experiment. The limit of detection was 0.7 N ($\Delta R = 3\sigma$).
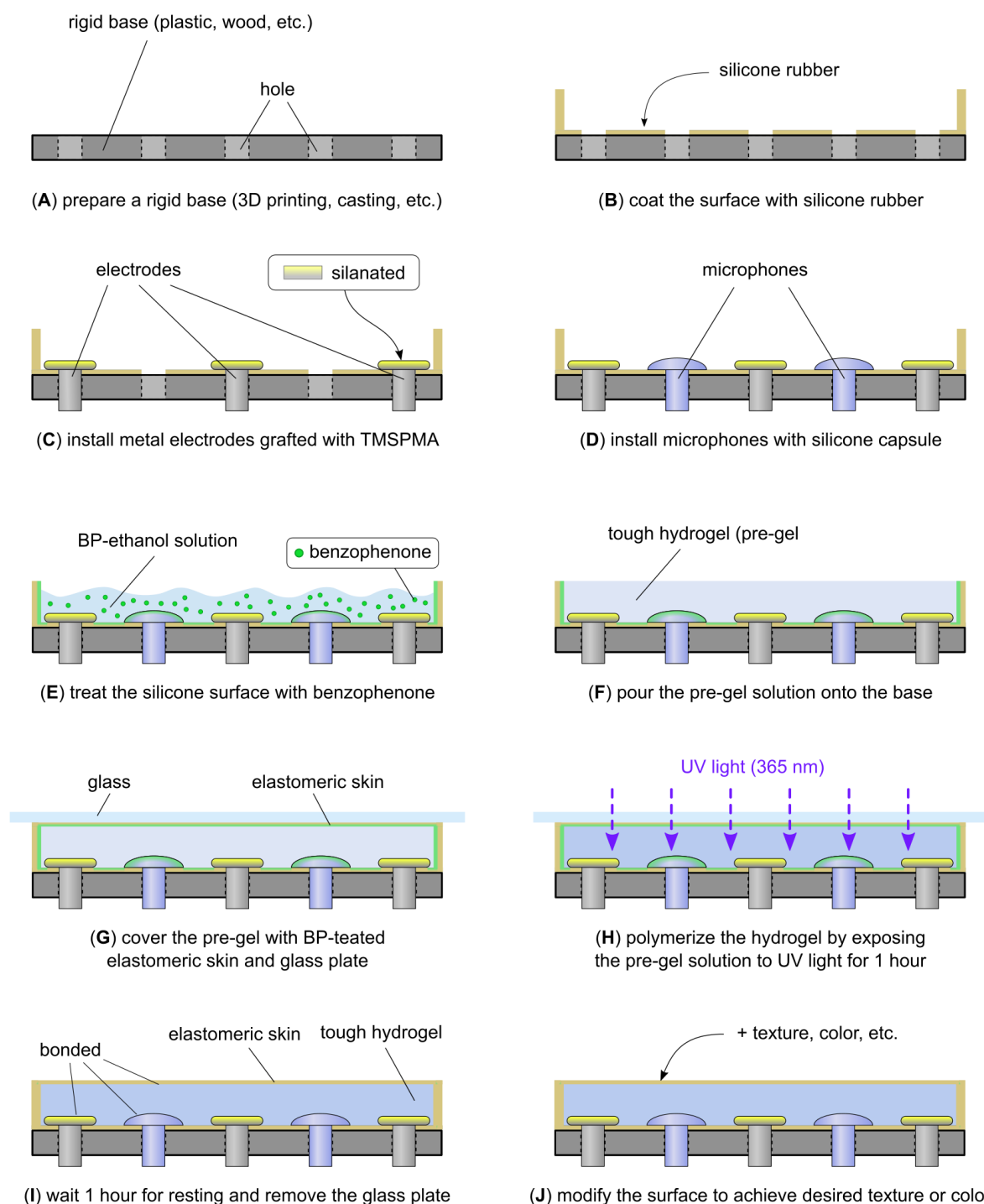
Fig. S5. Fabrication process of the biomimetic robotic skin. (**A**-**B**) The rigid base was prepared through 3D printing, casting, etc., and it was coated with silicone rubber (i.e., dragon skin 20, smooth-on). (**C**-**E**) The electrodes and microphones were installed on the rigid base, and the silicone parts were treated with 10 wt.% benzophenone-ethanol solution. (**F**) The pregel solution of tough hydrogel was then poured onto the base. (**G**) The pregel solution was also covered with a BP-treated elastomeric skin, and the glass plate was placed on the elastomeric skin tightly to prevent contact between the hydrogel and oxygen and to maintain the shape of the hydrogel. (**H**-**I**) The hydrogel was polymerized by exposing it to UV light (365 nm) for 1 hour, the glass plate was removed 1 hour after the polymerization. (**J**) Additional steps can be followed to modify the surface to achieve desired texture or color. Owing to the benzophenone absorbed in the silicone surface, the hydrogel and silicone is strongly bonded. The metal electrodes were also strongly bonded with hydrogel since its surface was grafted with TMSPMA.
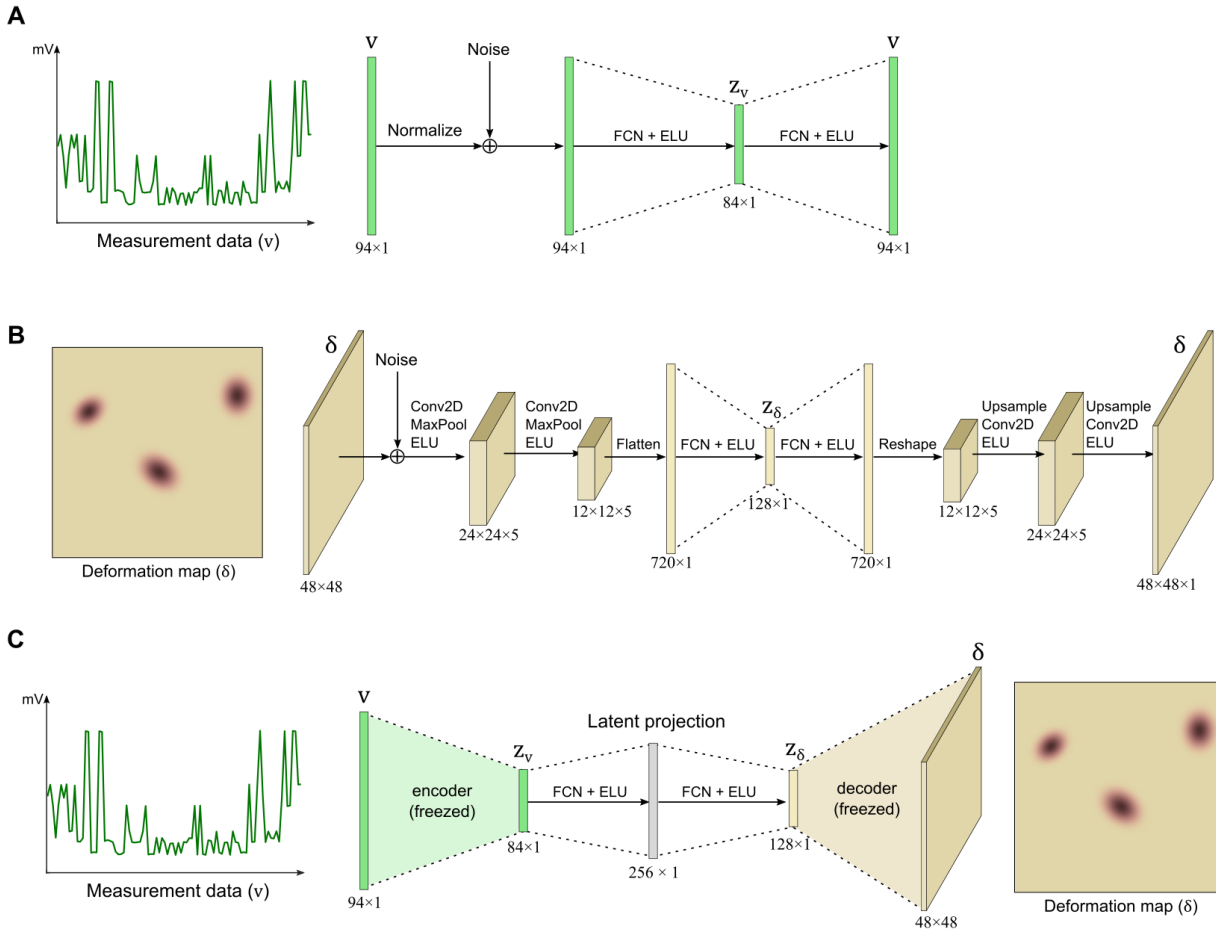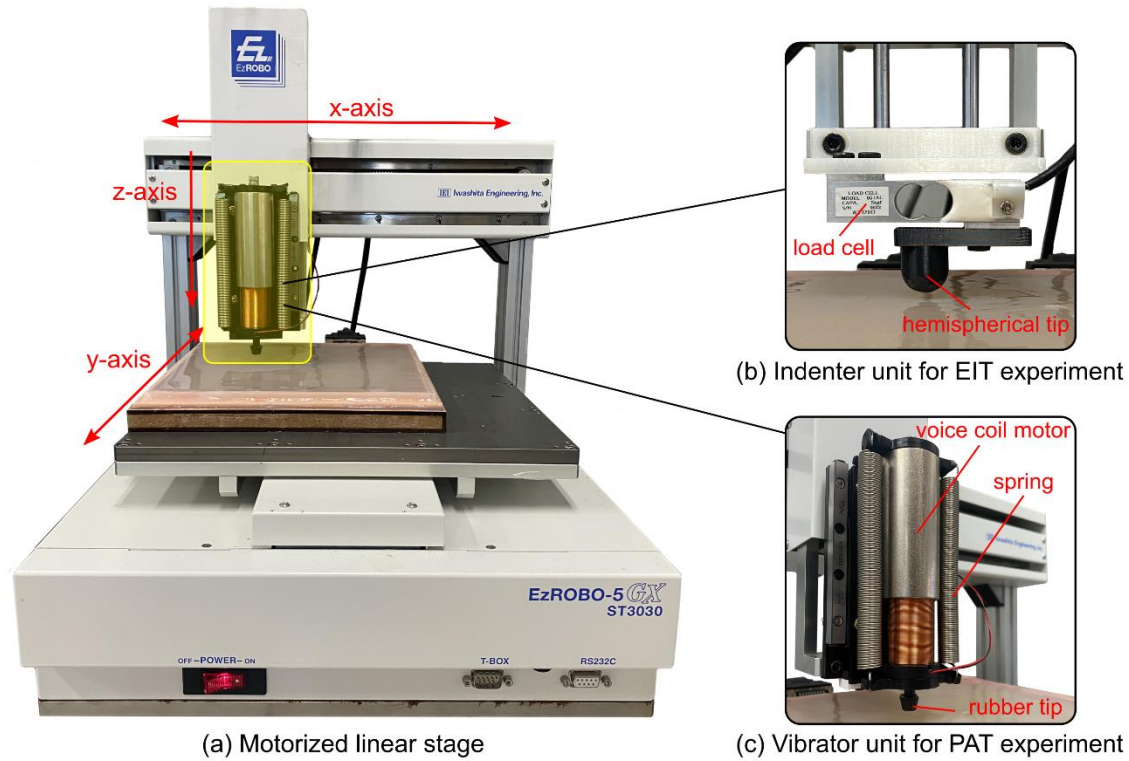
Fig. S6. Electrical impedance tomography based on a deep neural network to reconstruct the deformation map. (**A**) Denoising autoencoder for learning latent representation of measurement data; (**B**) Convolutional autoencoder for learning latent representation of deformation map; and (**C**) Projection between two latent space (from z_v to z_δ) for reconstructing the deformation map from measurement data.
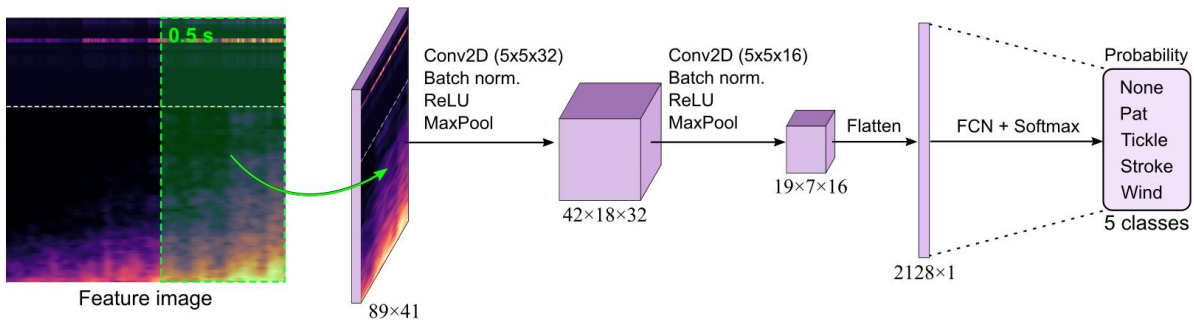
Fig. S7. Classification of dynamic tactile stimuli using a convolutional neural network. The feature image was obtained by concatenating the intensity histories of multichannel vibration signals and the spectrogram from the most significant channel. The size of the multichannel intensity history and the spectrogram are 25×41 and 64×41, so the size of the feature image is 89×41. The length of time window is 0.5 second. The spatiotemporal pattern of the vibration is then searched by convolutional neural network with ReLU activation function. Finally, the extracted features are flattened and go through the FCN with the SoftMax layer to classify the tactile stimuli into five classes (i.e., pat, tickle, stroke, wind, and none).
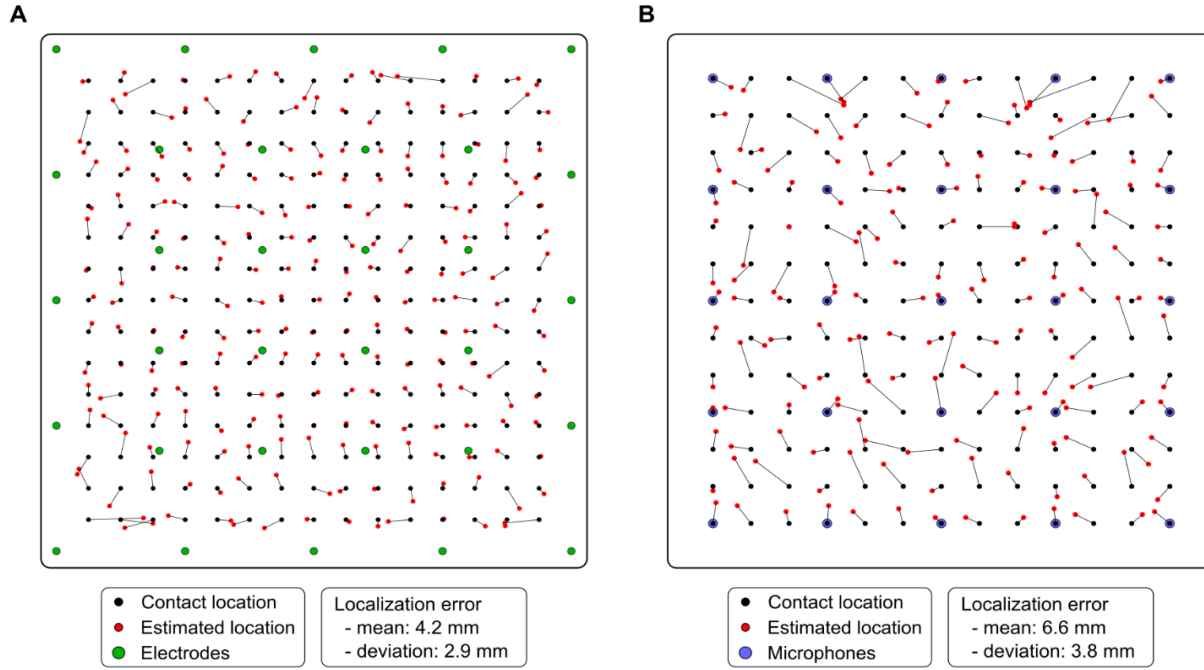
Fig. S8. Contact localization performance. (a) Contact localization result using a DNN-based EIT reconstruction algorithm. The green circles indicate the location of electrodes. The black and red circles indicate the true and estimated position of contact, respectively. Corresponding pairs are connected to each other by a black line. The contact location is defined as a centroid obtained by using the deformation map as weights. The result shows that the localization error is 4.2 mm ± 2.9 mm, which is remarkable value considering the number of the electrodes. This suggests that tactile super-resolution has been successfully implemented at low electrode densities through DNN-based EIT; (b) Contact localization result using PAT algorithm. The blue circles indicate the location of microphones. The black and red circles indicate the true and estimated position of contact, respectively. Corresponding pairs are also connected to each other by a black line. The contact location is defined as the pixel that minimizes the loss defined in the vibration decaying model. The loss map is calculated in 200-by-200 rectangular grid. The result shows that localization error is 6.6 mm ± 3.8 mm. The contact localization using PAT is less accurate than the result of EIT, but it is still noticeable considering the placement density of the microphones.

x-axis

z-axis

y-axis

EzROBO-5 *GX*
ST3030

(a) Motorized linear stage

load cell

hemispherical tip

(b) Indenter unit for EIT experiment

voice coil motor

spring

rubber tip

(c) Vibrator unit for PAT experiment

Fig. S9. Experiment setup for evaluating contact localization performance. (a) Motorized 3D linear stage is equipped with an indenter or a vibrator; (b) Indenter unit consists of load cell and hemispherical tip with a diameter of 15 mm. This unit is used to evaluate EIT-based contact localization performance; and (c) Vibrator unit consists of a voice coil motor, a spring, and a rubber tip. This unit is used to evaluate PAT-based contact localization performance.
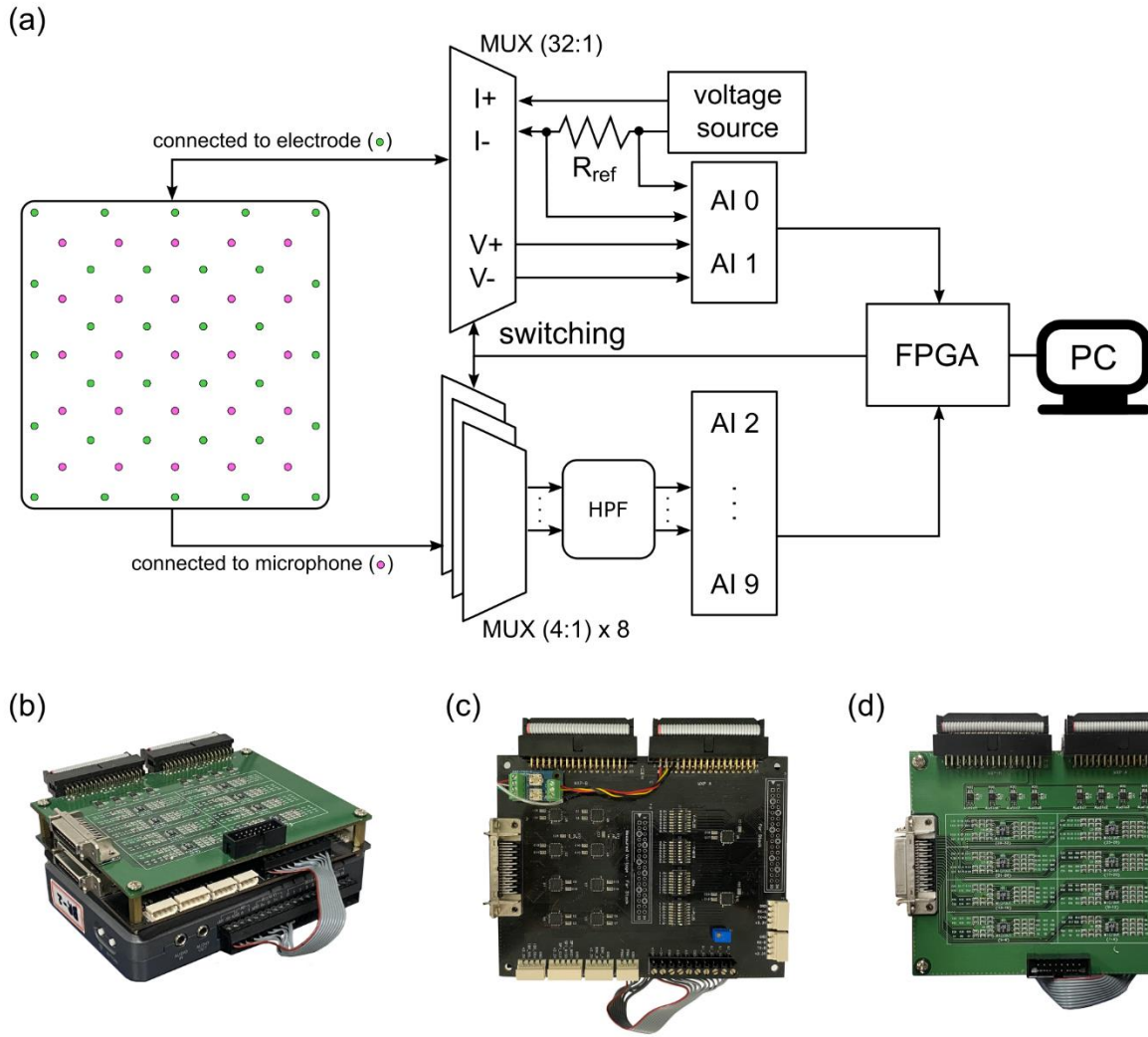
Fig. S10. Measurement device for multi-modal tactile sensing based on tomographic imaging. (a) Scheme of field-programmable gate array (FPGA)-based measurement system for electrical impedance tomography and passive acoustic tomography. The FPGA is used for both of electrode switching and data acquisition. The measured data are filtered inside the FPGA and sent to the host through the buffer (DMA FIFO). The typical idle power consumption is only 2.6 W, and the sensor itself consumes only 6 mW approximately; (b) DAQ stacked with the boards; (c) EIT board with multiplexors; and (d) PAT board with analog filters and multiplexors.
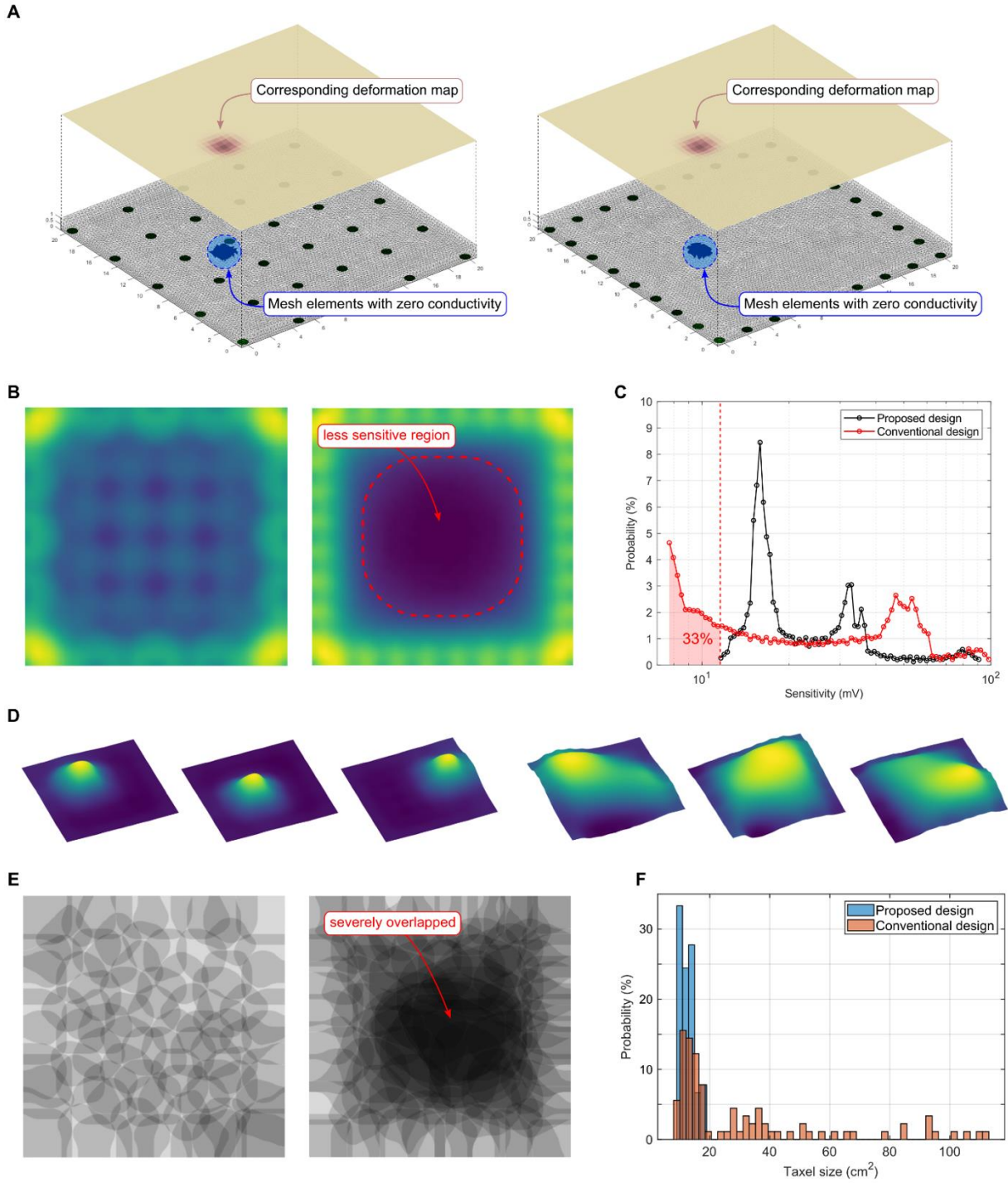
Fig. S11. Comparison of sensor characteristics between EIT-based tactile sensors with different electrode arrangements. (**A**) Examples of mesh models with conductivity perturbation (left: proposed design, right: conventional design). For simulation, the mesh elements corresponding to the indented portion were set to have a zero-conductivity value; (**B**) Sensitivity map obtained from transfer impedance matrices (left: proposed design, right: conventional design). The conventional design has an insensitive region at the central region; (**C**) Histogram of sensitivity distribution (black: proposed design, red: conventional design). The area of the insensitive region is about 33 % of the total area; (**D**) Examples of similarity surfaces obtained from proposed design (left three images) and conventional design (right three images); (**E**) Virtual taxels obtained from each mesh model (left: proposed design, right: conventional design). The conventional design has severely overlapping virtual taxels in the central region, implying its inferior spatial acuity; (**F**) Histogram of the size of the virtual taxels.
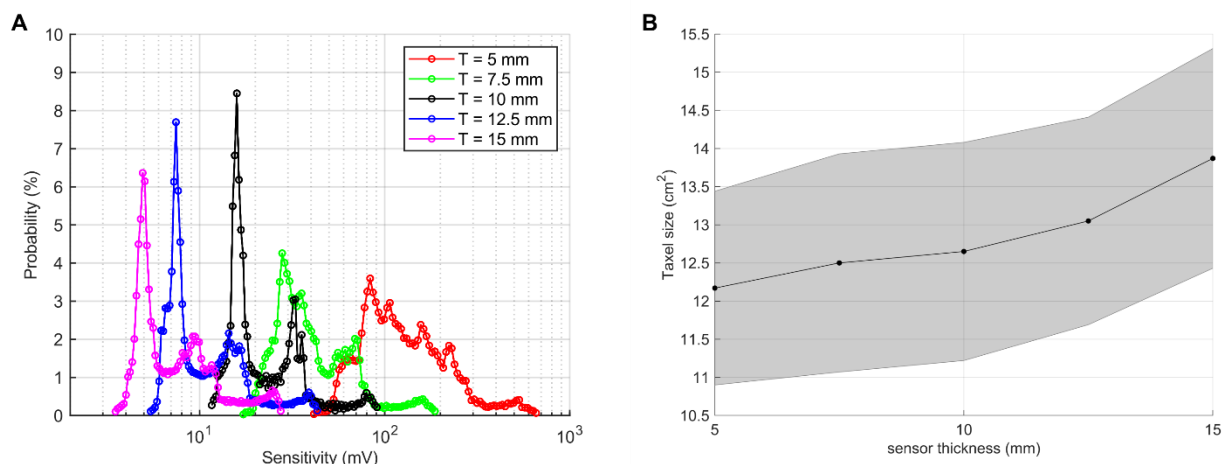
Fig. S12. Influence of sensor thickness on tactile sensing characteristics. (a) Sensitivity distribution by sensor thickness. (b) Size of virtual taxels by sensor thickness
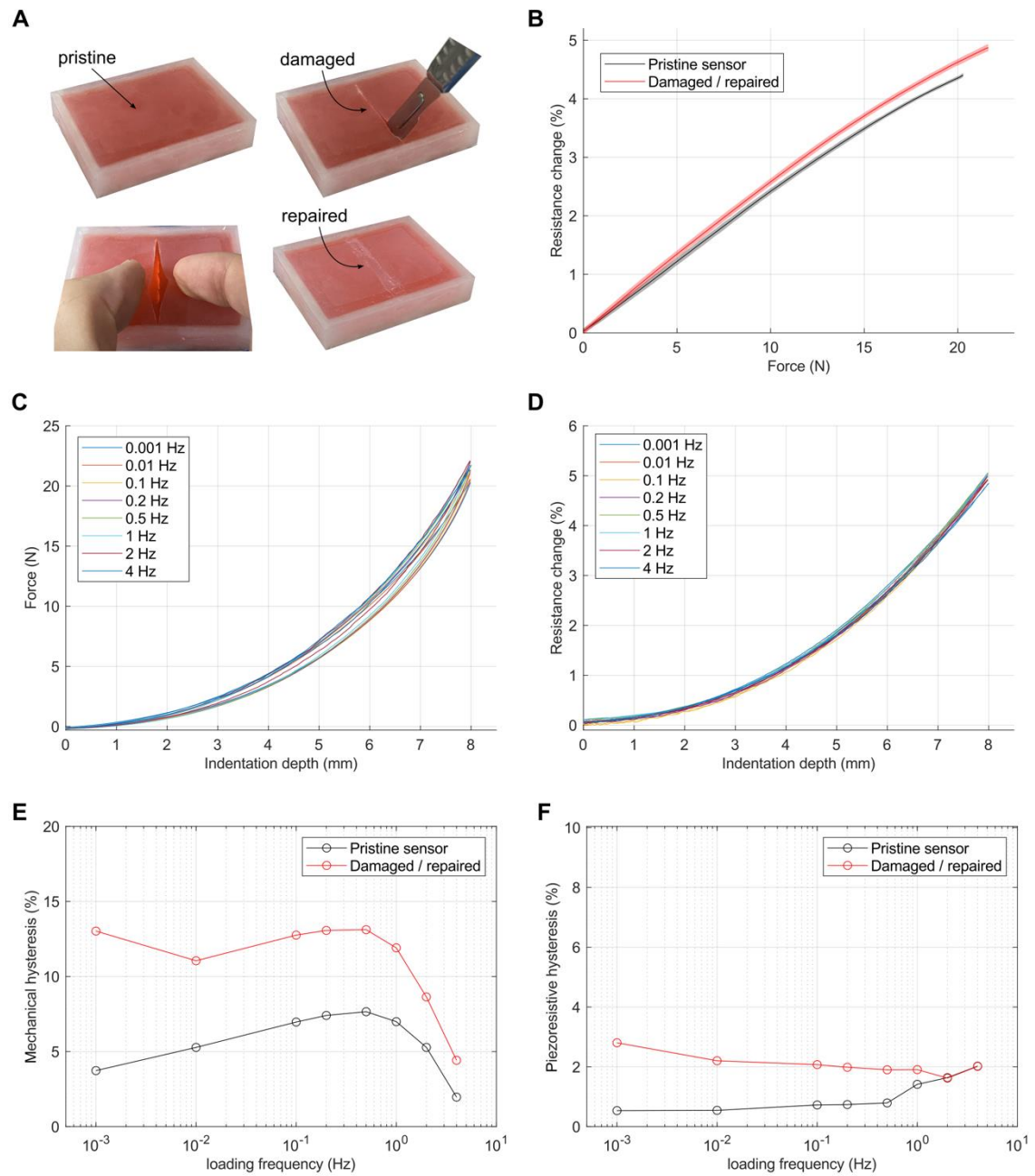
Fig. S13. Changes in piezoresistive properties due to damage and repair. (**A**) Specimen for the experiment (pristine, damaged, widened, and repaired). This specimen is identical to the specimen used for the cyclic loading test (Fig. S4). The specimen was cut with a surgical knife and repaired by applying chitosan topohesive and silicone adhesive; (**B**) Relationship between force and normalized resistance change. The electrical connection was perfectly restored and not changed even under the external force. The loading/unloading curve is slightly changed after damage and repair, but the trend of the curve was almost the same as before the damage; (**C**) Relationship between indentation depth and force; (**D**) Relationship between indentation depth and normalized resistance change; (**E**) Mechanical hysteresis; and (**F**) Piezoresistive hysteresis by loading frequency show that the specimens have more hysteretic characteristics after damage and repair.
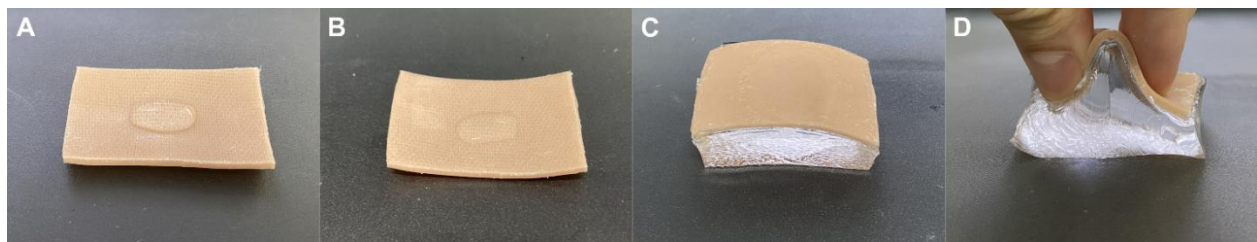
Fig. S14. Additive fabrication of hydrogel on a hydrogel-coated elastomer (**A**) Inner side of the elastomeric skin; (**B**) Inner side of the elastomeric skin coated with PAAm hydrogel; (**C**) Additive fabrication of hydrogel on a hydrogel-coated surface. The bulk hydrogel is polymerized by thermo-initiator; (d) The bonding between the elastomeric skin and the hydrogel was maintained even under deformation such as lifted skin fold (pinch).
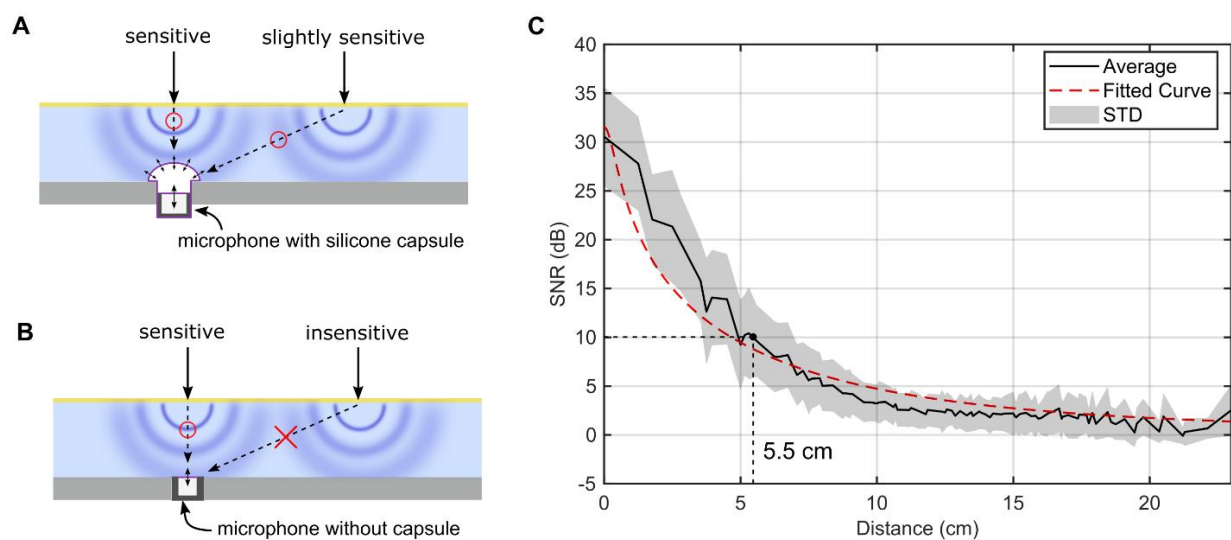
Fig. S15. Receptive field of microphone encased with silicone capsule (**A**) Large and omnidirectional receptive field due to silicone capsule; (**B**) Small receptive field due to the lack of silicone capsule; (**C**) Relationship between the vibration propagation distance and the SNR of the measured vibration